

ELECTRO-MECHANICAL MODELING AND ANALYSIS FOR THE
VIBRATION OF UNBALANCED AND MISALIGNED MOTOR
ROTOR

By
Yousef Adnan Yousef Smadi

Supervisor
Dr. Bassem Al-Bedoor, Prof.

This Thesis was Submitted in Partial Fulfillment of the Requirements for
the Master's Degree of Science in Mechanical Engineering.

Faculty of Graduate Studies
The University of Jordan

May, 2009

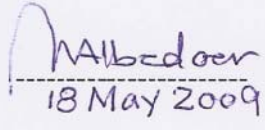
COMMITTEE DECISION

This thesis (**Electro-Mechanical Modeling and Analysis for the Vibration of Unbalanced and Misaligned Induction Motor Rotor**) was successfully defended and approved on: 14/05/2009.

Examination Committee:

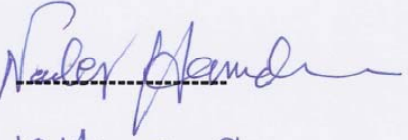
Signature.

Dr. Bassem O. Al-Bedoor, (Supervisor)
Prof. of Applied Mechanics.



18 May 2009

Dr. Mohammad Nader Hamdan, (Member)
Prof. of Applied Mechanics.



18 May, 2009

Dr. Ahmad Al-Qaisieh, (Member)
Assoc. Prof. of Applied Mechanics.



Dr. Abdul Hai Al-Alami, (Member)
Assist. Prof. of Applied Mechanics.
(The Hashemite University)



18th May 2009

تعتمد كلية الدراسات العليا
هذه النسخة من الرسالة
التوقيع:.....التاريخ: 14/5/09

Dedication

I would like to dedicate this work to my **PARENTS** who made me to what I am now; their vision for me is always my inspiration, they suffered a lot for me, they made me insist to succeed, they taught me how to walk again after the drop.

DAD and MOM, this is one step forward for me, you are making it.

Yousef

Acknowledgment

I would like to acknowledge my supervisor “**Dr. Bassem Al-Bedoor**” who creates the idea of this research, make me attached to this field and did great efforts to make it come true. All the thanks and appreciation to you Dr. Bassem.

Also I would like to thank my closest friend “*Aboud*” for his endless support and encouragement.

Finally, all my friends’ supports are highly recognized and appreciated.

Yousef Smadi

TABLE OF CONTENT

Content	Page
Committee Decision	ii
Dedication	iii
Acknowledgment	iv
Table of Content	v
List of Tables	vii
List of Figures	viii
Nomenclature	x
Abstract	xii
Ch.1 Introduction	
1.1 Description of the Problem	1
1.2 Previous Work	3
1.3 Current Status	10
1.4 Objectives	11
1.5 Thesis overview	12
Ch.2 Mathematical Modeling	
2.1 Introduction	13
2.2 Induction Motor Model	14
2.3 Mechanical Model of the Rotor	20
2.3.1 Kinetic Energy Expressions	22
2.3.2 Potential Energy Expressions	24
2.3.3 The Equation of Motion	25
2.4 Coupled System Model	29
Ch.3 Simulation Setup / Results	
3.1 Simulation Setup	31
3.1.1 Electrical System	34
3.1.2 Mechanical System	36

Content	Page
3.1.3 Combined System (Mechanical and Electrical)	37
3.2 Simulation Results	39
3.2.1 Electrical System Simulation Results	39
3.2.2 Mechanical System Simulation Results	44
3.2.3 Combined System Simulation Results	48
3.2.3.1 Unbalanced Rotor Results	49
3.2.3.2 Unbalanced and Misaligned Rotor Results	56
3.3 Parametric Study of Unbalance Mass and Misalignment Force	63
Ch.4 Discussion of Results	
4.1 Electrical System Simulation	65
4.2 Mechanical System Simulation	67
4.3 Combined System Simulation	69
4.3.1 Unbalanced Rotor Simulation	70
4.3.2 Misaligned and Unbalanced Rotor Simulation	72
4.4 Parametric Study of Unbalance Mass and Misalignment Force Simulation	75
Ch.5 Conclusion and Recommendations	
5.1 Conclusions	76
5.2 Recommendations	78
5.3 Future Work Recommendations	78
References	79
Abstract (in Arabic)	81

LIST OF TABLES

Table Number and Name	Page
Table 3.1.1: Mechanical System Data	36
Table 3.3.1: Values of Motor Current Spectra with Mass Unbalance	63
Table 3.3.2: Values of Motor Current Spectra with Rotor Misalignment.	63

LIST OF FIGURES

Figure Number and Name	Page
Figure 2.2.1: Polyphase winding and d-q equivalent	16
Figure 2.3.1: Schematic of the motor shaft disk system	20
Figure 2.3.2: Coordinate system and the deformation system configuration	21
Figure 3.1.1: System Configuration of Three Phase Induction Motor	34
Figure 3.1.2: Mechanical System of Unbalanced Rotor	35
Figure 3.1.3: The Total System of the Coupled Motor Rotor	38
Figure 3.2.1: Induction Motor Speed in RPM	39
Figure 3.2.2: Induction Motor Electromagnetic Torque	40
Figure 3.2.3: Induction Motor Stator Current	40
Figure 3.2.4: Stator Current Spectrum of Induction Motor Subjected to Constant Load Torque	41
Figure 3.2.5: Stator Current Spectrum of Induction Motor Subjected to Sinusoidal Load Torque of Amplitude (25 N.m) with Frequency (25 Hz)	41
Figure 3.2.6a: Stator Current Spectrum of Induction Motor Subjected to Sinusoidal Load Torque of Amplitude (25 N.m) with Frequency (200 Hz).	42
Figure 3.2.6b: Stator Current Spectrum of Induction Motor Subjected to Sinusoidal Load Torque of Amplitude (25 N.m) with Frequency (250 Hz).	42
Figure 3.2.6c: Stator Current Spectrum of Induction Motor Subjected to Sinusoidal Load Torque of Amplitude (25 N.m) with Frequency (300 Hz).	43
Figure 3.2.5: Rotor Input Torque	44
Figure 3.2.6: Rotor Speed in RPM	45
Figure 3.2.7: Rotor Torsional Deflection	45
Figure 3.2.8: Rotor Lateral Deflection	46
Figure 3.2.8a: Rotor Lateral Deflection (Zoomed View)	46
Figure 3.2.9: Rotor Lateral Deflection in XY Plane	47
Figure 3.2.10: Rotor Lateral Deflection Frequency Spectrum	47
Figure 3.2.11: Motor Current Frequency Spectrum for Healthy Rotor	48
Figure 3.2.12: Unbalanced Rotor Displacement in X Direction vs. Time	49
Figure 3.2.12a: Unbalanced Rotor Displacement in X Direction vs. Time (Zoomed View)	50

Figure Number and Name	Page
Figure 3.2.13: Unbalanced Rotor Displacement in Y Direction vs. Time	50
Figure 3.2.13a: Unbalanced Rotor Displacement in Y Direction vs. Time (Zoomed View)	51
Figure 3.2.14: Unbalanced Rotor Displacement in X Direction Spectrum	51
Figure 3.2.15: Unbalanced Rotor Displacement in Y Direction Spectrum	52
Figure 3.2.16: Unbalanced Rotor Displacement in XY Plain	52
Figure 3.2.17: Motor Stator Current Spectrum for Unbalanced Rotor	53
Figure 3.2.18: Motor Stator Current Spectrum for Unbalanced Rotor in Logarithmic Scale	53
Figure 3.2.19: Motor Stator Current Gain Spectrum for Unbalanced Rotor	54
Figure 3.2.20: Stator Current Spectrum for 8 Poles Induction Motor (715 rpm) with Unbalanced Rotor	54
Figure 3.2.21: Stator Current Spectrum for 16 Poles Induction Motor (357.5 rpm) with Unbalanced Rotor	55
Figure 3.2.22: Unbalanced and Misaligned Rotor Displacement in X Direction vs. Time	57
Figure 3.2.22a: Unbalanced and Misaligned Rotor Displacement in X Direction vs. Time (Zoomed View)	57
Figure 3.2.23: Unbalanced and Misaligned Rotor Displacement in Y Direction vs. Time	58
Figure 3.2.23a: Unbalanced and Misaligned Rotor Displacement in Y Direction vs. Time (Zoomed View)	58
Figure 3.2.24: Unbalanced and Misaligned Rotor Displacement in X Direction Spectrum	59
Figure 3.2.25: Unbalanced and Misaligned Rotor Displacement in Y Direction Spectrum	59
Figure 3.2.26: Unbalanced and Misaligned Rotor Displacement in XY Plain	60
Figure 3.2.27: Motor Stator Current Spectrum for Unbalanced and Misaligned Rotor	60
Figure 3.2.28: Motor Stator Current Spectrum for Unbalanced and Misaligned Rotor in Logarithmic Scale	61
Figure 3.2.29: Motor Stator Current Gain Spectrum for Unbalanced and Misaligned Rotor	61
Figure 3.2.30: Stator Current Spectrum for 8 Poles Induction Motor (715 rpm) with Unbalanced and Misaligned Rotor	62
Figure 3.2.31: Stator Current Spectrum for 16 Poles Induction Motor (357.5 rpm) with Unbalanced and Misaligned Rotor	62
Figure 3.3.1: Motor Current Spectra Value vs. Rotor Unbalance Mass	64
Figure 3.3.2: Motor Current Spectra Value vs. Rotor Misalignment	64

NOMENCLATURE

V_{sA}, V_{sB}, V_{sC} :	Stator three phase voltages.
V_{ra}, V_{rb}, V_{rc} :	Rotor three phase voltages.
I_{sA}, I_{sB}, I_{sC} :	Stator three phase currents.
I_{ra}, I_{rb}, I_{rc} :	Rotor three phase currents.
L_{ss}, L_{rr} :	Stator and rotor self inductance.
L_s, L_r :	Stator or rotor phase mutual inductance.
L_{sr} :	Stator and rotor mutual inductance.
R_s, R_r :	Stator and rotor resistances.
p :	Differential operator.
ω_b :	Voltage line frequency in rad/sec.
θ_r :	Rotor angle. ($\theta_{r1} = \theta_r + \frac{2\pi}{3}$, $\theta_{r2} = \theta_r + \frac{4\pi}{3}$)
i_{sq} :	Stator current in q axis.
i_{sd} :	Stator current in d axis.
i_o :	Stator current in zero neutral point.
i_{sa} :	Stator current in a axis.
i_{sb} :	Stator current in b axis.
i_{sc} :	Stator current in c axis.
N :	The number of pole pairs.
θ :	rigid body rotation angle.
ψ :	Torsional deflection angle.
XY :	Is the inertial reference frame.
$X^m Y^m$:	Is the body coordinate system of the motor shaft which is rotating with the torsionally un-deformed system.
xy :	Is the body coordinate system of the disk which is attached to the disk and exhibits all its motions.
J_M :	Is the motor mass moment of inertia.
M :	Is the rotor modal mass.
J_D :	Is the disk mass moment of inertia.

m_u :	Is the unbalance mass.
$\dot{\mathbf{R}}_e$:	Is the velocity vector of the unbalance mass in the inertial reference frame.
T_L :	Is the load torque on the motor.
ω :	Is the motor shaft speed.
v_l :	Is the line voltage.
i_l :	Is the line current.
ϕ :	Is the phase shift between the line voltage and line current.
$\cos\phi$:	Is the motor power factor.
η :	Is the motor efficiency.
T_e :	Is the electromagnetic torque.
T_L :	Is the load torque.
T_f :	Is the friction torque.
B :	Is the number of the coupling bolts.
K_b :	Is the effective stiffness of each bolt.
δ :	Is the vertical misalignment at the coupling.
Ω :	Is the reference rotor speed.
t :	Is the time.

ELECTRO-MECHANICAL MODELING AND ANALYSIS FOR THE VIBRATION OF UNBALANCED AND MISALIGNED MOTOR ROTOR

By
Yousef Adnan Yousef Smadi

Supervisor
Dr. Bassem Al-Bedoor, Prof.

ABSTRACT

Mathematical modeling for three phase induction motor coupled with unbalanced rotor at one stage and unbalanced misaligned rotor in the other stage, mathematical models for electrical and mechanical were combined to obtain the total coupled model. Computer numerical simulation was done using MATLAB/Simulink commercial software package. The solution of the coupled mathematical model was achieved based on predicative-corrective numerical integration algorithm Runga-Kutta integration method. The results showed that rotor unbalance can be detected in motor stator current frequency spectrum as two side bands apart from the current frequency by twice the rotor frequency (2X), where as the rotor misalignment can be detected as two side bands around the current frequency apart from it by one, three and five rotor frequency (1X, 3X and 5X). The value of motor stator current spectra in mass unbalance case is non-linearly proportional to mass unbalance value where it is linearly proportional to misalignment force.

CHAPTER ONE

INTRODUCTION

1.1 Description of the Problem

Rotating machines have become wide spread in industries across the world, covering many areas of process and production industries. The safe, smooth and efficient running of these machines has been counterweighed by the need for reliable and continuous operation. This has called for a heavy reliance on advances and development in maintenance strategies from Run-to-Fail to Preventive Maintenance (PM) and also Predictive Maintenance (PdM) or what is known as Condition Based Maintenance (CBM) today. The above techniques all converge into a broad set of paradigms known as Condition Monitoring, which means that there are critical parameters in need to be measured, processed and interpreted, such that they reflect the condition of the machine and drive the maintenance action through pinpointing the reason behind the malfunction (diagnostics).

There are many methods devised to perform the task of condition monitoring (CM). For example there are acoustic condition monitoring, thermal condition monitoring and the vibration measurement. The most widely used method in determining machine condition is vibration measurements, Penrose (2008). This method usually determines the severity and possible causes of machine problems such as unbalance, misalignment, vanes problems, looseness, etc, using vibrational transducers that acquire the vibration signal from the device at hand and compares it with a previously recorded signature of a healthy device. Vibration monitoring is very crucial, however it is considered to have secondary (indirect) effects when electrical

motors and generators are involved. Moreover, vibration measurement is not always possible when there is an accessibility problem.

Over the last 15 years, Penrose (2008), researchers have started efforts to find a system that complements the vibration measurement or sometimes can replace it. The idea started by monitoring the motor / generator current signature analysis (MCSA) based on the principle that vibration extracts some energy from the main source; this means that it will be reflected on the electrical current signal which dynamically impacts the power of the motor / generator.

Motor current signature monitoring systems along with the advances in signal processing have allowed electrical problems and flaws (e.g. broken rotor bars) to be predicted and identified before imminent breakdowns and with high confidence. Such problems will eventually result in a noticeable and sometimes detrimental unbalance of the rotating load or a misalignment problem of the rotating shaft.

In electrical motors, especially in induction motors, there is an inevitable interaction between its electrical and mechanical parts, known as the electromechanical coupling, where the supplied current is used to provide rotation to the rotor itself. Thus, electrical energy is converted into mechanical energy manifested by the rotation of the rotor, and any change in the electrical conditions will reflect on the mechanical conditions and vice versa.

1.2 Previous Work

As a natural start in research and development, researchers usually try to investigate the accomplishment of others in the research field of interest. Consequently, the problem of using motor current signature as a diagnostics tool has attracted the attention of many researches where some of these researches are documented through journal publications and/or conference presentations and others were not documented due to different reasons.

Binbouzid (1999) investigated the reliability of the electrical current as a diagnostic tool for motor health. In his paper he addressed the application of motor current spectral analysis for the detection and localization of abnormal electrical and mechanical conditions that indicate, or may lead to, a failure of induction motors. In his experiments he used an advanced signal processing technique (high resolution spectral analysis) which directed him to a result that the stator current high-resolution spectral analysis can be used as a tool for the induction motors faults detection.

Riley *et al.* (1999), studied the relationship between the vibration and the current harmonic of the electrical motors. In their experiments they used a new motor with external vibration and used a motor with bearing wear. The results they achieved from their experiments showed that the RMS vibration sum and the RMS current sum are tightly correlated, and this correlation implies that the current spectrum can be used to evaluate motor vibration.

A review of induction motors signature analysis as a medium for fault detection was conducted by Benbouzid (2000), in which he attempted to review fundamentals, main results, and practical applications of the MCSA used for induction motors faults

detection. His work was directed to build more confidence in MCSA and will be helpful to those who are interested in understanding the powerful capability of MCSA.

Al-Bedoor (2001), has developed a mathematical model that describes the coupled torsional and lateral vibration of an unbalanced rotor based on Lagrangian dynamics. His numerical simulation results showed energetic interaction between the rotor lateral and torsional vibration, and system response at 1X, 2X and 3X showed how energy flows between lateral and torsional vibration according to the system natural frequencies.

Bellini *et al.* (2002), monitored large induction motor cage condition to detect the rotor bar breakage, their diagnosis based on the Motor Current Signature Analysis (MCSA) especially on the two sideband current components near the fundamental line frequency that appear in the current power spectrum when a rotor bar-ring breakage occurs. Their experimental tests in laboratory confirmed the effectiveness of this diagnostic method.

Korde (2002), studied the On-Line motor condition monitoring using the electrical current signature analysis. He derived current signals and converted it from time domain to the frequency domain using Fast Fourier Transformer (FFT) analyzer which gave him many peaks (harmonic) in the signal. Analyzing those harmonics with motor condition monitoring enabled him to identify many motor problems and faults.

Liang *et al.* (2002), demonstrated that generalized motor model can be used to simulate induction motor faults to high degree of accuracy. This was done using computer simulation and then verified by experiment. Their investigation was based on voltage drop in one line fault detection from one side and broken one rotor bar from the

other side compared to normal healthy motor. The experimentally obtained results verified the simulation results.

Al-Hussain (2003), studied the dynamic stability and the effect of angular misalignment of two rigid rotors connected through a flexible mechanical coupling. Stability criteria was obtained using Liapunov's direct method through successive partial derivation of Hamiltonian. System stability condition was achieved based on Hamiltonian matrix, and the closed form whirl stability conditions are presented in terms of dimensionless stability criteria.

A detailed review that covers most of the conducted research is by Thomson and Gilmore (2003). Wherein they summarized that the motor current can be efficiently used for the detection of motor rotor broken bars, abnormal air gap eccentricity and shorted turns in low voltage stator windings. They came up with a conclusion that in the motor current spectrum, if the side bands of slipping frequency - slipping frequency is the result of multiplication of motor slip (s), synchronous speed (N_s) and the pole pairs of the windings (p) - around the main line frequency exceed a certain ratio relative to the main line frequency, then there is broken rotor bars. The gain of -40 dB of motor stator current side bands will indicate the existence of broken rotor bars.

Current signature analysis of induction motor mechanical faults by wavelet packet decomposition was conducted by Ye *et al.* (2003), New feature coefficients for induction motor mechanical faults are obtained by WPD of the stator current. The feature coefficients differentiate the healthy and faulty conditions with an obvious difference.

Improving the signal data acquisition in MCSA was introduced by Costa *et al.* (2004). New technique for suppressing the fundamental component of the squirrel cage

induction motor stator current signal is proposed. The fundamental component has been estimated by the recursive Fourier algorithm. Acquisition and suppression of the fundamental component are performed in real time. This technique has been applied to detect broken cage bars in an induction motor.

A new algorithm for use in transient motor current signature analysis has been introduced and applied to the detection of broken rotor bars in induction machines by Douglas *et al.* (2004). The algorithm was able to extract a single non-stationary sinusoid embedded within a non-stationary waveform. This is then applied to the transient inrush current of an induction motor and a wavelet analysis is conducted on the balance of the current.

Kar and Mohanty (2004), studied the possibility to replace the conventional condition monitoring for a multi-stages transmission gear box with a Motor Current Signature Analysis (MCSA). Their study was concerned only with the second gear fault detection. These studies lead them to a result that Motor Current Signature Analysis (MCSA) with discrete wavelet transform (DWT) is a good replacement for the conventional condition monitoring.

A detailed model of induction machines including saturation effect and extendable for fault analysis was set by Nandi (2004). This model was able to reproduce saturated related higher order harmonics in the machine line current, experimental results, however, show that, due to machine constructional imbalance and voltage unbalance, third harmonic line current components can indeed be presented, which also will influence the predicted higher harmonic components.

In addition Penrose has published a series of publications on MCSA; some applications of MCSA were discussed in his paper Penrose (2004), in which he

emphasized on the capability of MCSA in motor prognosis and diagnosis. The complexity of the diagnostics process depends on many factors. It can be noticed from Penrose work's that he as many others has concentrated on studding the frequency spectrums of some practical cases. Very few have executed mathematical modeling to control the factors that affect the MCSA spectrums.

Bearing fault detection via autoregressive stator current modeling was conducted by Stack *et al.* (2004). They presented a method for performing stator current based bearing condition monitoring. This was carried out based on isolating the non-bearing faults components from stator current.

Al-Bedoor *et al.* (2005), presented a technical approach for machinery health monitoring using machinery electrical parameters and verified mathematical models. They monitored the three phase electrical current and voltage for an induction motor and linked this monitoring with a verified mathematical model, wherein the parameters are obtained from the measurements of the machine train containing the induction motor. After that the electrical signature abnormalities was used as an indication for the mechanical problems. Case studies and success stories are also presented.

The frequency components of the stator current have been analytically and experimentally analyzed by Henao *et al.* (2005). They proved that the obtained analytical frequencies in the stator spectrum can be related to the experimental ones for normal operation and under rotor bar faults. The fact that the frequency components induced by rotor asymmetry are present in normal operation can be assumed as the inherent unbalance of the induction machine rotor cage reflected in the stator current spectrum. This result is very interesting for the optimization of the information given by the stator current.

A review of condition monitoring and fault diagnosis of electrical motors was conducted by Nandi *et al.* (2005). Based on their study it was clear from various literature that noninvasive MCSA is by far the most preferred technique to diagnose faults. However, theoretical analysis and modeling of machine faults are indeed necessary to distinguish the relevant frequency components from the others that may be present due to time harmonics, machine saturation, etc. Other techniques for fault detection based on axial flux-based measurements, vibration analysis, transient current, and voltage monitoring, etc. have also been discussed. A section on automated fault detection has also been included.

Jung *et al.* (2006) diagnosed 3.7 kW and 30 kW three phase squirrel cage induction motors having four types of faults such as breakage of rotor bars and end rings, short circuit of stator windings, bearing cracks, and air-gap eccentricity using the Motor Current Signature Analysis (MCSA). They found that the Motor Current Signature Analysis (MCSA) has a problem in the performance and accuracy of any motor diagnosis system, and therefore they used advanced signal and data processing algorithms. They achieved results from their experiments which confirmed the successful operation of their system which is composed from the Motor Current Signature Analysis (MCSA) with the advanced signal data processing.

Lees (2007), investigated the misalignment in rigidly coupled rotors, the equation of motion of a machine with a coupled alignment fault using purely liner model was derived. Analytical and numerical solutions for some simple cases were also carried out. These solutions showed that the liner model generate responses at harmonics of shaft speed caused by interaction between torsional and flexural effects.

As noted from the literature review presented above, none of the researchers - to the best of the author's knowledge - have studied the effect of unbalance and misalignment on motor current signature. This provides the launching point of this research effort. Also, the instances where researchers have conducted simulations delving to the core of the electrical/mechanical systems interaction were rare, since most have relied on experimentation. These experiments mostly relied on breaking some of the rotor bars with no real focus on the unbalance or misalignment problems.

1.3 Current Status

Based on the previously reviewed researches a number of points on the issue of MCSA as a tool for diagnostic have emerged:

- a. The MCSA is nonintrusive method and can be very useful for reduced cost monitoring as well as for applications with accessibility problems.
- b. Most of the conducted research has concentrated on the problem of broken bars.
- c. Still very few mathematical models are available in the open literature.
- d. The problems of unbalance and misalignment are still not fully understood when it comes to their signature in MCSA technique.
- e. No mathematical model that can differentiate between unbalance and misalignment is available.

1.4 Objectives

This master thesis research has the following objectives:

- a. To utilize a suitable mathematical model that allows the coupling of the electro/mechanical system and use a simulation tool to verify it.
- b. To investigate the problems of mechanical unbalance and misalignment using theoretical and simulation tools used to detect the electrical current signature in mechanical trains driven by three phase induction motors.
- c. To decide and find out the sensitivity of the motor current signature analysis as compared to mechanical vibration measurement.
- d. To come up with guidelines for and define the limitations of the detection of mechanical unbalance and misalignment using current signature analysis.

1.5 Thesis overview

This thesis will be broken down into five chapters. The current chapter, chapter 1, includes an introduction of the work, highlighting its importance and original contribution. It also provided a literature survey on previous work and endeavors to formulate current signatures as a viable method of fault detection, and a natural way to couple the electro/mechanical sides of the problem.

The second chapter contains the mathematical basis of the models used throughout this research effort. These mathematical models were of extreme importance in setting up and executing later simulations using software tools.

The third chapter reports on the specific parameters and simulation effort used to model the unbalance and misalignment problems. Specific assumptions were stated and the main model was built and tested using MATLAB/Simulink commercial software. A special section presented the results obtained from running the model, where appropriate output files and graphs were generated and displayed.

The fourth chapter was dedicated to the discussion of the results obtained from running the model. This is followed by chapter five which includes the conclusions for using these techniques in the field along with recommendations for future work.

CHAPTER TWO

MATHEMATICAL MODELING

2.1 Introduction

Induction motors are the most widely used electrical drives over the world. Between 40 to 50 percent of generated industrial energy is consumed in induction motors according to Thomson and Gilmore (2003). This is due to its advantages over other electrical drive types. Its main advantage is that it does not have contact brushes between stator and rotor, reducing the wear and tear maintenance needed and eliminating the generated spark is a fire hazard in flammable areas. In addition induction motors are known for their silent operation, their relative low cost, simple design and suitable operating curve over a wide range of applications requirements.

Induction motors can be classified based on the supplied power type as three phase motor (industrial type) and single phase motors (home application type), or they can also classified based on their rotor construction as squirrel cage rotor (most common type) and wound rotor type. In this research, only three phase squirrel cage induction motor will be considered.

An induction motor has some minor disadvantages; High starting current caused by the absent of back electromagnetic current is one of them where relatively complicated speed control is another one, so most of induction motors are mostly used in constant speed applications, but motor speed may be reduced below its nominal operating values due to mechanical loading according to its operation curve.

2.2 Induction Motor Model

The parameters involved when simulating systems that utilize induction motors can be divided into two main categories. The first can be classified under the electrical model of the induction motor itself, and the second -which will be demonstrated in the next section- is the mechanical model of the rotor coupled with the motor and is currently represents the useful load that the motor is trying to rotate.

The three phase induction motor mathematical model will be based on generalized rotating field theory; Liang *et al* (2002), and by considering the following fairly acceptable assumptions:

- Infinite magnetic permeability of iron is considered and very small and smooth air-gap.
- State of operation remains far from magnetic saturation.
- Constant self-inductance and mutual-inductance between stator or rotor phases.
- Mutual-inductance between the stator and the rotor windings are functions of the rotor position.
- Space magnetic motive force and flux profiles are considered to be sinusoidal distributed and higher harmonics are negligible.
- The rotor bars are electrically insulated as far as the iron surfaces are concerned.

The matrix form of the adopted model can be written as: Liang *et al* (2002).

$$\begin{bmatrix} V_{sA} \\ V_{sB} \\ V_{sC} \\ V_{ra} \\ V_{rb} \\ V_{rc} \end{bmatrix} = \begin{bmatrix} R_s + pL_{ss} & pL_s & pL_s & pL_{sr}\cos\theta_r & pL_{sr}\cos\theta_{r1} & pL_{sr}\cos\theta_{r2} \\ pL_s & R_s + pL_{ss} & pL_s & pL_{sr}\cos\theta_{r2} & pL_{sr}\cos\theta_r & pL_{sr}\cos\theta_{r1} \\ pL_s & pL_s & R_s + pL_{ss} & pL_{sr}\cos\theta_{r1} & pL_{sr}\cos\theta_{r2} & pL_{sr}\cos\theta_r \\ pL_{sr}\cos\theta_r & pL_{sr}\cos\theta_{r2} & pL_{sr}\cos\theta_{r1} & R_r + pL_{rr} & pL_r & pL_r \\ pL_{sr}\cos\theta_{r1} & pL_{sr}\cos\theta_r & pL_{sr}\cos\theta_{r2} & pL_r & R_r + pL_{rr} & pL_r \\ pL_{sr}\cos\theta_{r2} & pL_{sr}\cos\theta_{r1} & pL_{sr}\cos\theta_r & pL_r & pL_r & R_r + pL_{rr} \end{bmatrix} \begin{bmatrix} I_{sA} \\ I_{sB} \\ I_{sC} \\ I_{ra} \\ I_{rb} \\ I_{rc} \end{bmatrix} \quad (2.2.1)$$

Where:

V_{sA}, V_{sB}, V_{sC} : Stator three phase voltages.

V_{ra}, V_{rb}, V_{rc} : Rotor three phase voltages.

I_{sA}, I_{sB}, I_{sC} : Stator three phase currents.

I_{ra}, I_{rb}, I_{rc} : Rotor three phase currents.

L_{ss}, L_{rr} : Stator and rotor self inductance.

L_s, L_r : Stator or rotor phase mutual inductance.

L_{sr} : Stator and rotor mutual inductance.

R_s, R_r : Stator and rotor resistances.

p : Differential operator.

θ_r : Rotor angle. ($\theta_{r1} = \theta_r + \frac{2\pi}{3}$, $\theta_{r2} = \theta_r + \frac{4\pi}{3}$)

According to Okoro (2003) this model can be reduced to a simpler model using what is called D-Q Axis Transformation Theory, explained by Okoro as follows: “The d-q axis transformation eliminates the mutual magnetic coupling of the phase-winding, thereby making the magnetic flux linkage of one winding independent of the current in the other winding. This system of transformation allows both polyphase windings in the stator and rotor of an inductance machine to be viewed from a common reference frame, which may rotate at any angular speed or remain fixed to the stator. Generally, the reference frame can also be considered to be rotating at any arbitrary angular speed.” (Okoro 2003).

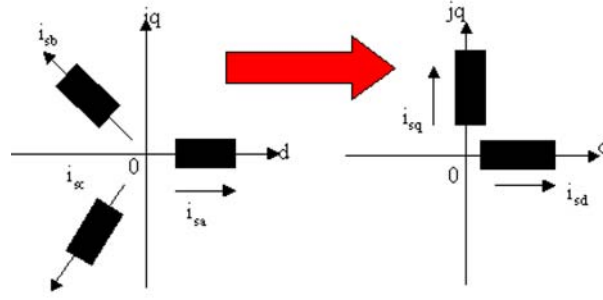


Figure 2.2.1: Polyphase winding and d-q equivalent.

Based on this theory the number of variables sets can be reduced from 3 down to 2 as shown in figure (2.1.1). In other words this theory changes the mathematical model of induction motor from statuary frame reference to the rotor frame reference. This leads to the following mathematical formulation:

$$\begin{bmatrix} i_{sq} \\ i_{sd} \\ i_0 \end{bmatrix} = [C] \begin{bmatrix} i_{sa} \\ i_{sb} \\ i_{sc} \end{bmatrix} \quad (2.2.2)$$

where:

i_{sq} : Stator current in q axis.

i_{sd} : Stator current in d axis.

i_0 : Stator current in zero neutral point.

i_{sa} : Stator current in a axis.

i_{sb} : Stator current in b axis.

i_{sc} : Stator current in c axis.

$$[C] = \frac{2}{3} \begin{bmatrix} \cos \theta & \cos(\theta - \frac{2\pi}{3}) & \cos(\theta - \frac{4\pi}{3}) \\ \sin \theta & \sin(\theta - \frac{2\pi}{3}) & \sin(\theta - \frac{4\pi}{3}) \\ \frac{1}{2} & \frac{1}{2} & \frac{1}{2} \end{bmatrix} \quad (2.2.3)$$

And so the system inverse can be written as:

$$\begin{bmatrix} i_{sa} \\ i_{sb} \\ i_{sc} \end{bmatrix} = [C]^{-1} \begin{bmatrix} i_{sq} \\ i_{sd} \\ i_0 \end{bmatrix} \quad (2.2.4)$$

$$[C]^{-1} = \begin{bmatrix} \cos \theta & \sin \theta & 1 \\ \cos(\theta - \frac{2\pi}{3}) & \sin(\theta - \frac{2\pi}{3}) & 1 \\ \cos(\theta - \frac{4\pi}{3}) & \sin(\theta - \frac{4\pi}{3}) & 1 \end{bmatrix} \quad (2.2.5)$$

Under balanced voltage condition the stator voltage of a three phase induction motor can be expressed as:

$$V_{as} = \sqrt{2}V \cos(\omega_b t) \quad (2.2.6)$$

$$V_{bs} = \sqrt{2}V \cos(\omega_b t - \frac{2\pi}{3}) \quad (2.2.7)$$

$$V_{cs} = \sqrt{2}V \cos(\omega_b t + \frac{2\pi}{3}) \quad (2.2.8)$$

where:

ω_b : is the voltage line frequency in rad/sec.

These voltages are related to the d-q frame of reference by Eq. (2.1.2):

$$\begin{bmatrix} V_{sq} \\ V_{sd} \end{bmatrix} = [E] \begin{bmatrix} V_{as} \\ V_{bs} \\ V_{cs} \end{bmatrix} \quad (2.2.9)$$

where:

$$[E] = \frac{2}{3} \begin{bmatrix} \cos \theta & \cos(\theta - \frac{2\pi}{3}) & \cos(\theta - \frac{4\pi}{3}) \\ \sin \theta & \sin(\theta - \frac{2\pi}{3}) & \sin(\theta - \frac{4\pi}{3}) \end{bmatrix} \quad (2.2.10)$$

Then Eq. (2.2.9) can be simplified using trigonometric identities whereby to take the form:

$$V_{sq} = \sqrt{2}V \cos(\theta - \omega_b t) \quad (2.2.11)$$

$$V_{sd} = \sqrt{2}V \sin(\theta - \omega_b t) \quad (2.2.12)$$

Those two equations (2.2.11 & 2.2.12) can be used in any reference frame by making a suitable choice for (θ); if ($\theta = \theta_r$) then the voltage will be in the rotor reference frame, if ($\theta = 0$) then the voltage will be in stationary reference frame, otherwise, for ($\theta = \omega t$) synchronously rotating reference frame results.

The following assumptions should be made in order to achieve the conventional machine model:

- The machine is symmetrical with a liner air-gap and magnetic circuit.
- Saturation effect is neglected.
- Skin-effect and temperature effect are neglected.
- Harmonic content of the mmf wave is neglected.
- The stator voltages are balanced.

Then the system motor model yields the following equation:

$$\begin{bmatrix} V_{qs} \\ V_{ds} \\ 0 \\ 0 \end{bmatrix} = \begin{bmatrix} (R_s + L_s p) & \omega L_s & L_m p & \omega L_m \\ -\omega L_s & (R_s + L_s p) & -\omega L_m & L_m p \\ L_m p & (\omega - \omega_r) L_m & (R_r + L_r p) & (\omega - \omega_r) L_r \\ -(\omega - \omega_r) L_m & L_m p & -(\omega - \omega_r) L_r & (R_r + L_r p) \end{bmatrix} \begin{bmatrix} i_{qs} \\ i_{ds} \\ i_{qr} \\ i_{dr} \end{bmatrix} \quad (2.2.13)$$

where:

$$L_s = L_{ls} + L_m \quad (2.2.14)$$

$$L_r = L_{lr} + L_m \quad (2.2.15)$$

$$p = \frac{d}{dt} \quad (2.2.16)$$

For numerical simulation eq. (2.2.13) can be rewritten as:

$$p[\mathbf{i}] = -[\mathbf{L}](\mathbf{R} + \omega_r[\mathbf{G}])[\mathbf{i}] + [\mathbf{L}]^{-1}[\mathbf{V}] \quad (2.2.17)$$

where:

$$[\mathbf{V}] = [V_{qs} \quad V_{ds} \quad 0 \quad 0]^T \quad (2.2.18)$$

$$[\mathbf{R}] = \begin{bmatrix} R_s & 0 & 0 & 0 \\ 0 & R_s & 0 & 0 \\ 0 & 0 & R_r & 0 \\ 0 & 0 & 0 & R_r \end{bmatrix} \quad (2.2.19)$$

$$[\mathbf{L}] = \begin{bmatrix} L_s & 0 & L_m & 0 \\ 0 & L_s & 0 & L_m \\ L_m & 0 & L_r & 0 \\ 0 & L_m & 0 & L_r \end{bmatrix} \quad (2.2.20)$$

$$[\mathbf{G}] = \begin{bmatrix} 0 & L_s & 0 & L_m \\ -L_s & 0 & -L_m & 0 \\ 0 & 0 & 0 & 0 \\ 0 & 0 & 0 & 0 \end{bmatrix} \quad (2.2.21)$$

$$[\mathbf{i}] = [i_{qs} \quad i_{ds} \quad i_{qr} \quad i_{dr}]^T \quad (2.2.22)$$

Then the electromagnetic torque T_e can be expressed as:

$$T_e = \frac{3}{2}NL_m(i_{qs}i_{dr} - i_{ds}i_{qr}) \quad (2.2.23)$$

where:

N: is the number of pole pairs.

2.3 Mechanical Model of the Rotor

Mechanical model is obtained based on disk-shaft arrangement driven by three-phase induction motor as shown in figure (2.3.1). Shaft is supported by two fluid bearings and coupled to the motor by mass less flexible coupling; the model was developed based on the following six assumptions, Al-Bedoor, (2001):

- The model adopts the simple Jeffcot's approach that considers the system as massive rigid disk mounted midway between the bearings on a mass less flexible shaft.
- The moving mass (M), is not only the mass of the disk but the modal mass that corresponds to the first lateral mode of the system.
- The approach is valid below the second lateral critical speed.
- The lateral stiffness is the shaft flexural stiffness which is assumed to be relatively small compared to the bearings stiffness.
- The bearings have only linear viscous damping effect.
- The Gyroscopic effects due to disk spinning are neglected.

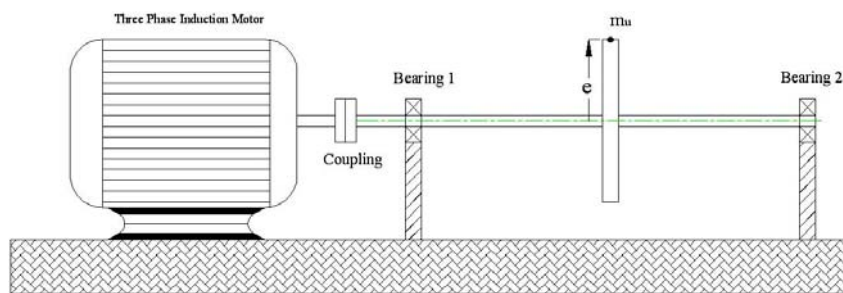


Figure 2.3.1: Schematic of the motor shaft disk system.

The system has four degrees of freedom; first one is the rigid body rotation angle (θ), the second degree of freedom is the torsional deflection angle (ψ), the last two degrees

of freedom are the orthogonal lateral deflection of the disk geometrical center (X, Y) . As shown in figure (2.3.2), the coordinate systems used to develop the model are:

XY : Is the inertial reference frame.

$X^m y^m$: Is the body coordinate system of the motor shaft which is rotating with the torsionally un-deformed system.

xy : Is the body coordinate system of the disk which is attached to the disk and exhibits all of its motions.

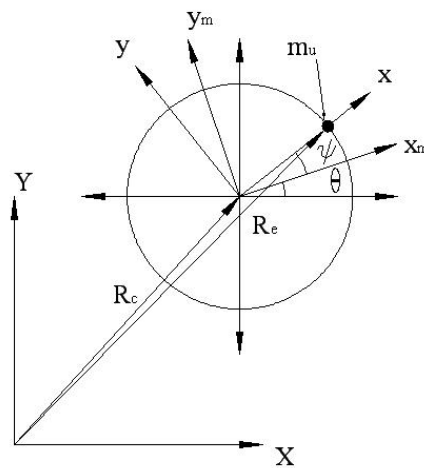


Figure 2.3.2: Coordinate system and the deformation system configuration.

The mass unbalance (m_u) is located at the middle of the disk width and at end of disk radius eccentricity vector (e) with respect to body coordinate system (xy). Lagrangian dynamics in the inertial coordinate system was used to develop the model.

2.3.1 Kinetic Energy Expressions

The disk shaft system kinetic energy is the summation of the motor, the disk and the mass unbalance kinetic energies; which can be expressed as the following:

$$K.E. = \frac{1}{2}M(\dot{X}^2 + \dot{Y}^2) + \frac{1}{2}J_D(\dot{\theta} + \dot{\psi})^2 + \frac{1}{2}J_M\dot{\theta}^2 + \frac{1}{2}m_u\dot{\mathbf{R}}_e^T \cdot \dot{\mathbf{R}}_e \quad (2.3.1)$$

where:

J_M : Is the motor mass moment of inertia.

M : Is the rotor modal mass.

J_D : Is the disk mass moment of inertia.

m_u : Is the unbalance mass.

$\dot{\mathbf{R}}_e$: Is the velocity vector of the unbalance mass in the inertial reference frame.

The global position vector of the mass unbalance can be written as:

$$\mathbf{R}_e = [A(\theta)][A(\psi)]\mathbf{e} \quad (2.3.2)$$

where:

$[A(\theta)]$: Is the rotational transformation matrix from the motor coordinate system to the inertial frame (XY).

$[A(\psi)]$: Is the rotational transformation matrix from disk coordinate system (xy) to motor coordinate system.

$$[A(\theta)] = \begin{bmatrix} \cos\theta & -\sin\theta \\ \sin\theta & \cos\theta \end{bmatrix} \quad (2.3.3)$$

$$[A(\psi)] = \begin{bmatrix} \cos\psi & -\sin\psi \\ \sin\psi & \cos\psi \end{bmatrix} \quad (2.3.4)$$

Based on the fact that (ψ) is very small angle as it represents torsional deformation angle measured with respect to the motor coordinate system, then $A(\psi)$ can be linearized to be:

$$[A(\psi)] = \begin{bmatrix} 1 & -\psi \\ \psi & 1 \end{bmatrix} \quad (2.3.5)$$

By differentiating Eq. (3.2), the velocity vector of the mass unbalance in the inertial reference frame can be obtained as:

$$\dot{R}_e = \dot{\theta}[A_\theta(\theta)][A(\psi)]e + \dot{\psi}[A(\theta)][A_\psi(\psi)]e \quad (2.3.6)$$

where:

$[A_\theta(\theta)]$ and $[A_\psi(\psi)]$ represent the derivatives $[d A(\theta) / d\theta]$ and $[d A(\psi) / d\psi]$ respectively.

After substituting $[A_\theta(\theta)]$ and $[A_\psi(\psi)]$ into Eq. (3.6) the velocity vector of the mass unbalance in the inertial reference frame can be obtained as:

$$\dot{R}_e = \begin{cases} \dot{X} - \dot{\theta}e_x(\sin\theta + \psi\cos\theta) - \dot{\theta}e_y(\cos\theta - \psi\sin\theta) - \dot{\psi}(e_x\sin\theta + e_y\cos\theta) \\ \dot{Y} + \dot{\theta}e_x(\cos\theta - \psi\sin\theta) - \dot{\theta}e_y(\sin\theta + \psi\cos\theta) + \dot{\psi}(e_x\cos\theta - e_y\sin\theta) \end{cases} \quad (2.3.7)$$

Where e_x and e_y are the mass unbalance initial position in x and y directions respectively, assumed starting from positive x direction ($\theta = 0$).

$$e_x = e \quad (2.3.7a)$$

$$e_y = 0 \quad (2.3.7b)$$

Substituting Eq. (3.7) into Eq. (3.1) will give:

$$\begin{aligned}
K.E. = & \frac{1}{2}(M + m_u)(\dot{X}^2 + \dot{Y}^2) + \frac{1}{2}m_u e^2 \dot{\theta}^2 (1 + \psi^2) + \frac{1}{2}m_u e^2 \dot{\psi}^2 - m_u \dot{X} \dot{\theta} [(e_x - \\
& \psi e_y) \sin \theta + (e_x \psi + e_y) \cos \theta] + m_u \dot{Y} \dot{\theta} [(e_x - \psi e_y) \cos \theta - (e_x \psi + e_y) \sin \theta] - \\
& m_u \dot{X} \dot{\psi} (e_x \sin \theta + e_y \cos \theta) + m_u \dot{Y} \dot{\psi} (e_x \cos \theta - e_y \sin \theta) + m_u e^2 \dot{\theta} \dot{\psi} + \frac{1}{2} J_M \dot{\theta}^2 + \\
& \frac{1}{2} J_D (\dot{\theta} + \dot{\psi})^2
\end{aligned} \tag{2.3.8}$$

2.3.2 Potential Energy Expressions

The system potential energy is the summation of the shaft bending strain energy and the torsional strain energy, it can be expressed as:

$$P.E. = \frac{1}{2} k_x X^2 + \frac{1}{2} k_y Y^2 + \frac{1}{2} k_T \psi^2 \tag{2.3.9}$$

2.3.3 The Equation of Motion

After substituting the kinetic energy and potential energy expressions into Lagrange's equation and performing the required differentiation and manipulation as the following, the system equation of motion will be as:

Lagrange's equation:

$$\frac{d}{dt} \left(\frac{\partial L}{\partial \dot{q}_i} \right) - \frac{\partial L}{\partial q_i} = F_i \quad i = 1,2,3,4 \quad (2.3.10)$$

where:

$$L = \text{K.E.} - \text{P.E.} \quad (2.3.10a)$$

$$q_1 = \theta \quad (2.3.10b)$$

$$q_2 = \psi \quad (2.3.10c)$$

$$q_3 = X \quad (2.3.10d)$$

$$q_4 = Y \quad (2.3.10e)$$

$$F_1 = F_\theta \quad (2.3.10f)$$

$$F_2 = F_\psi \quad (2.3.10g)$$

$$F_3 = F_X \quad (2.3.10h)$$

$$F_4 = F_Y \quad (2.3.10i)$$

Applying Lagrange's equation for first degree of freedom (θ):

$$\begin{aligned} [J_M + J_D + m_u e^2(1 + \psi^2)]\ddot{\theta} + [J_D + m_u e^2]\ddot{\psi} - m_u[(e_x - \psi e_y)\sin\theta + (\psi e_x + e_y)\cos\theta]\ddot{X} + m_u[(e_x - \psi e_y)\cos\theta - (\psi e_x + e_y)\sin\theta]\ddot{Y} + m_u\dot{\theta}\dot{Y}[(e_x - \psi e_y)\cos\theta + (\psi e_x + e_y)\sin\theta] - m_u\dot{\psi}\dot{X}(e_x\sin\theta + e_y\cos\theta) = F_\theta \end{aligned} \quad (2.3.11)$$

Applying Lagrange's equation for second degree of freedom (ψ):

$$\begin{aligned} [J_D + m_u e^2]\ddot{\theta} + [J_D + m_u e^2]\ddot{\psi} - m_u[e_x\sin\theta + e_y\cos\theta]\ddot{X} + m_u[e_x\cos\theta - e_y\sin\theta]\ddot{Y} + C_{\psi\psi}\dot{\psi} + (K_T - m_u e^2\dot{\theta}^2)\psi = F_\psi \end{aligned} \quad (2.3.12)$$

Applying Lagrange's equation for third degree of freedom (X):

$$\begin{aligned} -m_u[(e_x - \psi e_y)\sin\theta + (\psi e_x + e_y)\cos\theta]\ddot{\theta} - m_u[e_x\sin\theta + e_y\cos\theta]\ddot{\psi} + [M + m_u]\ddot{X} + C_{XX}\dot{X} + K_{XX}X + 2m_u\dot{\theta}\dot{\psi}(e_y\sin\theta - e_x\cos\theta) - m_u\dot{\theta}^2[(e_x - \psi e_y)\cos\theta - (\psi e_x + e_y)\sin\theta] = F_X \end{aligned} \quad (2.3.13)$$

Applying Lagrange's equation for fourth degree of freedom (Y):

$$\begin{aligned} m_u[(e_x - \psi e_y)\cos\theta - (\psi e_x + e_y)\sin\theta]\ddot{\theta} + m_u[e_x\cos\theta - e_y\sin\theta]\ddot{\psi} + [M + m_u]\ddot{Y} + C_{YY}\dot{Y} + K_{YY}Y - 2m_u\dot{\theta}\dot{\psi}(e_x\sin\theta + e_y\cos\theta) - m_u\dot{\theta}^2[(e_x - \psi e_y)\sin\theta + (\psi e_x + e_y)\cos\theta] = F_Y \end{aligned} \quad (2.3.14)$$

After arranging the system of equations in matrix form, the system will be:

$$\begin{bmatrix} m_{\theta\theta} & m_{\theta\psi} & m_{\theta X} & m_{\theta Y} \\ m_{\psi\theta} & m_{\psi\psi} & m_{\psi X} & m_{\psi Y} \\ m_{X\theta} & m_{X\psi} & m_{XX} & 0 \\ m_{Y\theta} & m_{Y\psi} & 0 & m_{YY} \end{bmatrix} \begin{bmatrix} \ddot{\theta} \\ \ddot{\psi} \\ \ddot{X} \\ \ddot{Y} \end{bmatrix} + \begin{bmatrix} 0 & 0 & 0 & 0 \\ 0 & C_{\psi\psi} & 0 & 0 \\ 0 & 0 & C_{XX} & C_{XY} \\ 0 & 0 & C_{YX} & C_{YY} \end{bmatrix} \begin{bmatrix} \dot{\theta} \\ \dot{\psi} \\ \dot{X} \\ \dot{Y} \end{bmatrix} + \begin{bmatrix} 0 & 0 & 0 & 0 \\ 0 & k_{\psi\psi} & 0 & 0 \\ 0 & 0 & k_{XX} & k_{XY} \\ 0 & 0 & k_{YX} & k_{YY} \end{bmatrix} \begin{bmatrix} \theta \\ \psi \\ X \\ Y \end{bmatrix} + \begin{bmatrix} Q_\theta \\ 0 \\ Q_X \\ Q_Y \end{bmatrix} = \begin{bmatrix} F_\theta \\ F_\psi \\ F_X \\ F_Y \end{bmatrix} \quad (2.3.15)$$

Where:

$$m_{\theta\theta} = J_M + J_D + m_u e^2 (1 + \psi^2) \quad (2.3.16)$$

$$m_{\psi\psi} = m_{\theta\psi} = m_{\psi\theta} = J_D + m_u e^2 \quad (2.3.17)$$

$$m_{\theta X} = m_{X\theta} = -m_u [(e_x - \psi e_y) \sin\theta + (e_x \psi + e_y) \cos\theta] \quad (2.3.18)$$

$$m_{\theta Y} = m_{Y\theta} = m_u [(e_x - \psi e_y) \cos\theta - (e_x \psi + e_y) \sin\theta] \quad (2.3.19)$$

$$m_{\psi X} = m_{X\psi} = -m_u [e_x \sin\theta + e_y \cos\theta] \quad (2.3.20)$$

$$m_{\psi Y} = m_{Y\psi} = m_u [e_x \cos\theta - e_y \sin\theta] \quad (2.3.21)$$

$$m_{XX} = m_{YY} = M + m_u \quad (2.3.22)$$

$$k_{\psi\psi} = k_T - m_u e^2 \dot{\theta}^2 \quad (2.3.23)$$

$$Q_\theta = 2m_u e^2 \psi \dot{\psi} \dot{\theta} \quad (2.3.24)$$

$$Q_X = 2m_u \dot{\theta} \psi (e_y \sin\theta - e_x \cos\theta) - m_u \dot{\theta}^2 [(e_x - \psi e_y) \cos\theta - (e_x \psi + e_y) \sin\theta] \quad (2.3.25)$$

$$Q_Y = -2m_u \dot{\theta} \psi (e_x \sin\theta + e_y \cos\theta) - m_u \dot{\theta}^2 [(e_x - \psi e_y) \sin\theta + (e_x \psi + e_y) \cos\theta] \quad (2.3.26)$$

As shown in Eq. (2.3.15), the inertia matrix -first matrix- is nonlinearly coupling the system degrees of freedom, damping and stiffness matrixes are linearly not coupled, and remaining nonlinear terms of the system are gathered in Q matrix.

Angular motion mass moment of inertia is represented in Eq. (2.3.16), the inertia coupling between θ and ψ and the torsional mass moment of inertia is expressed in Eq. (2.3.17), inertia coupling θ with X and θ with Y is expressed in Eq. (2.3.18) and Eq. (2.3.19) respectively, same thing for ψ with X and ψ with Y in Eq. (2.3.20) and Eq. (2.3.21), lateral motion mass of the system is in Eq. (2.3.22).

Torsional stiffness of the system is expressed in Eq. (2.3.23) which is affected by shaft torsional stiffness and nonlinearly related to mass unbalance position and rotor speed.

2.4 Coupled System Model

Electrical and mechanical systems can be coupled based on the fact that energy will be balanced between the two systems after coupling. In other words, electrical energy will be converted into mechanical energy through the induction motor, resulting mechanical energy will make the rotor motion, this fact can be expressed mathematically for steady state operation as the following:

$$Power = T_L \omega = \sqrt{3} v_l i_l * \cos \phi * \eta \quad (2.4.1)$$

where:

T_L : is the load torque on the motor.

ω : is the motor shaft speed.

v_l : is the line voltage.

i_l : is the line current.

ϕ : is the phase shift between the line voltage and line current.

$\cos \phi$: is the motor power factor.

η : is the motor efficiency.

All the terms in Eq. (2.4.1) are constants - assuming constant line voltage - except the load torque and in sequence the line current; *the load torque will be variable due to the variation in inertia tensor in the unbalanced and misaligned rotor*. Based on this the two models will be coupled by setting equal torque between electrical and mechanical systems.

$$J \frac{d^2\theta}{dt^2} = T_e - T_L - T_f \quad (2.4.2)$$

Where:

T_e : is the electromagnetic torque.

T_L : is the load torque.

T_f : is the friction torque.

With reference to Eq. (2.3.15), the load torque for the rotor under investigation can be expressed as:

$$m_{\theta\theta}\ddot{\theta} + m_{\theta\psi}\dot{\psi} + m_{\theta X}\ddot{X} + m_{\theta Y}\dot{Y} + Q_\theta = T_L \quad (2.4.3)$$

When reaching the steady state operation, $\frac{d^2\theta}{dt^2}$ will be zero and Eq. (2.4.3) will reduced to:

$$m_{\theta X}\ddot{X} + m_{\theta Y}\dot{Y} = T_L \quad (2.4.4)$$

Substituting from Eq. (2.3.18) and Eq. (2.3.19) for $m_{\theta X}$ and $m_{\theta Y}$, and from the mechanical simulation for \ddot{X} and \dot{Y} will result:

$$T_L = \sqrt{[-m_u(e \sin \theta)(-\omega^2 A \cos \omega t)]^2 + [m_u(e \cos \theta)(-\omega^2 A \sin \omega t)]^2} \quad (2.4.5)$$

where A is the mechanical vibration amplitude.

$$T_L = \sqrt{2} [m_u e A \omega^2 \sin \theta \cos \theta] = \sqrt{2} [m_{\theta X} \ddot{X}] \quad (2.4.5a)$$

Thus eq. (2.4.2) yields to Eq. (2.4.6) which will be solved by numerical simulation for the motor stator current values:

$$i_{qs}i_{dr} - i_{ds}i_{qr} = \frac{2\sqrt{2}}{3N L_m} [m_{\theta X} \ddot{X}] - T_f \quad (2.4.6)$$

CHAPTER THREE

SIMULATION SETUP / RESULTS

3.1 Simulation Setup

The simulation was divided into three main parts, in relation to the systems being simulated. The first system simulated was the electrical, in terms of applied load torque and its effect on the motor current. Secondly the mechanical system in terms of the applied torque and its effect on the rotational behavior was simulated. Finally the combined effect of both systems mentioned above was simulated with the addition of the effects of unbalance of the rotor disc and also an existing misalignment of the rotor shaft.

According to Lees (2007) the forces developed mainly because of the existence of shaft misalignment is a function of the frequency of the rotational speed and the misalignment deflection, δ . Other parameters are also cited, but their significance is not as apparent. During the course of this research, it was noted that due to the unbalance, δ is not expected to remain constant, rather it will match the frequency of the vibration caused by the unbalance in the rotating shaft. This frequency, when combined by multiplication by the sinusoidal term of the rotational frequency, as seen in equation 16 introduced by Lees (2007), will result in a variable lateral internal force acting on the rotating shaft having a frequency equal to twice the rotational frequency. This find highlights a lot of the experimental results found in the field with very few analytical or simulation data to fully explain it. Further experiments are, however, required to validate the data with specifically designed experiments.

In mathematical form this can be expressed as the following:

Equation 16 from Lees (2007) is:

$$F = \frac{BK_b\delta}{2} \begin{pmatrix} \cos \Omega t \\ \sin \Omega t \\ \delta \\ -\cos \Omega t \\ -\sin \Omega t \\ -\delta \end{pmatrix} \quad (3.1.1)$$

where:

B: is the number of the coupling bolts.

K_b : is the effective stiffness of each bolt.

δ : is the vertical misalignment at the coupling.

Ω : is the reference rotor speed.

t: is the time.

For the unbalanced rotor δ will variable in sinusoidal form as the following:

$$\delta = A \sin \Omega t \quad (3.1.2)$$

where A is dummy variable vibration amplitude caused by the unbalance.

Substituting in eq. (3.1.1):

$$F = A \sin \Omega t \cos \Omega t \quad (3.1.3)$$

Then:

$$F = A \sin 2\Omega t \quad (3.1.4)$$

Also, the capability of MATLAB/Simulink to simulate the input and output parameters of the mechanical model that will be described shortly was checked by verifying an analytical solution of the unbalanced rotor problem demonstrated in Al-Bedoor (2001), using the simulation features of the software.

A final stage of this research will be a parametric study focusing on changing the unbalance mass and the misalignment force and observing their effect on the amplitude of the frequency spectrum and its spikes of the unbalanced/misaligned rotor. It is worthwhile mentioning that the unbalance mass and misalignment force increase has to be significant, since the rotor itself is of large size. This is due to the limitation within MATLAB of the smallest available preset motor size model.

For all the above simulation, predictive-corrective numerical integration algorithm was used as built-in Runge-Kutta solver within MATLAB, listed under ODE4 function with a fixed time step. The fixed time step option was used since it lends itself to the later utilization of the Fast Fourier Transformation (FFT). The time step itself was chosen to equal (10^{-4}) seconds.

The version of MATLAB/Simulink used was 2007a for all the simulations conducted on all models in this research. The electrical model used was based on a series of preset values available within MATLAB/Simulink library.

3.1.1 Electrical System

The electrical system of the three phase induction motor under consideration was simulated within MATLAB/Simulink as detailed in figure (3.1.1).

The induction motor under consideration is 4 KW power and 1500 rpm rotating speed (actual 1430 rpm), 50 Hz input voltage frequency.

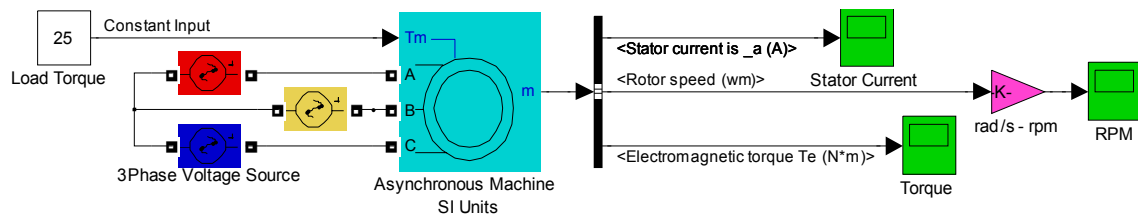


Figure 3.1.1: System Configuration of Three Phase Induction Motor.

The inputs to the motor were the three phase supply voltage as well as the load torque. The outputs were the shaft speed, the electromagnetic torque and one of the current phases of the stator. The supply voltage depends on the parameters of the motor, and in this particular case the voltage was chosen as 380 V (rms) with 50 Hz frequency. The sum of constant load torque and the friction torque was arbitrarily chosen to be 25 N.m, suiting the motor power.

3.1.2 Mechanical System

The mechanical system of the unbalanced rotor is shown in figure (3.1.2).

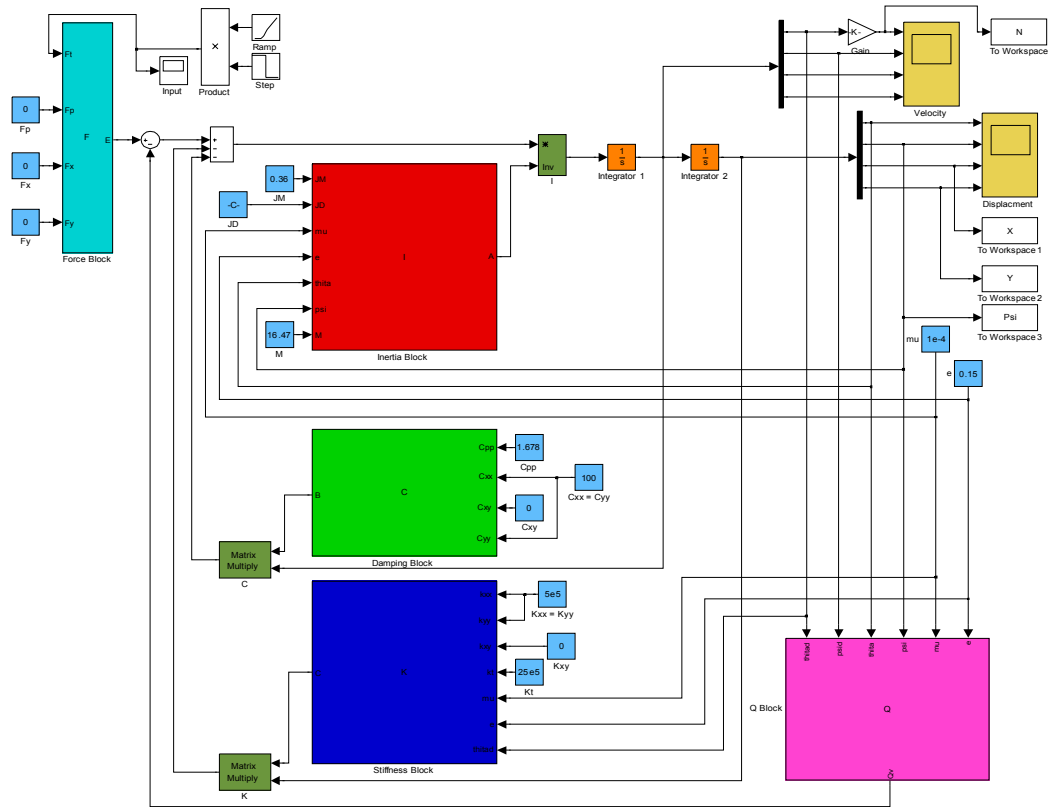


Figure 3.1.2: Mechanical System of Unbalanced Rotor.

To simulate the mechanical system of the rotor under consideration, the process was not as straight forward as was the case in the electrical system; since there is no single block exists that would describe the desired mechanical behavior of the rotor. Thus, many blocks from within Simulink library were combined to produce the desired effect. As seen in figure (3.1.2) the system was constructed using two integrators in series to produce the terms of velocity and position by starting the integration process from the acceleration of the system. The acceleration is the force divided by the inertia term, while the damping and stiffness are multiplied by the velocity and the displacement,

respectively. Nonlinear terms were added to compensate for any deviation of the simulation from realistic behavior.

The input to the mechanical system is the external torque supplied. Other parameters are shown in table (3.1.1), such as inertia, stiffness and damping. The outputs from the simulation are the rotational velocity of the rotor disc, the position of its center and its torsional deflection. The amplitude of the frequencies of the deflection of the disc centroid is also a desired parameter to observe to map the vibration of the disc to the rotational speed.

Table 3.1.1: Mechanical System Data.

Property	Value
Disk mass M	16.47 kg
Disk moment of inertia J_D	0.1861 kg.m ²
Motor moment of inertia J_M	0.36 kg.m ²
Shaft lateral stiffness k_{XX}, k_{YY}	5×10^5 N/m
Shaft torsional stiffness k_t	25×10^5 N/m
Imbalance mass m_u	1×10^{-4} kg
Imbalance eccentricity e	0.15 m
Lateral nodes damping ratio	0.0175
Torsional mode damping ratio	1.23×10^{-3}

3.1.3 Combined System (Mechanical and Electrical)

The two systems are combined together to obtain the motor current signature caused by the disc mechanical vibration, and thus warn against any misalignment or unbalance as a departure from a “healthy” vibration signature.

The combination can be achieved by matching the power between the two systems; electrical power is voltage times current, whereas mechanical power is speed times torque. Since the above mentioned parameters are interrelated, with the voltage and rotational speed are constant in the case of the induction motor. This leaves the torque and current as the interacting variables. Figure (3.1.3) below shows the block diagram used to simulate the combined system.

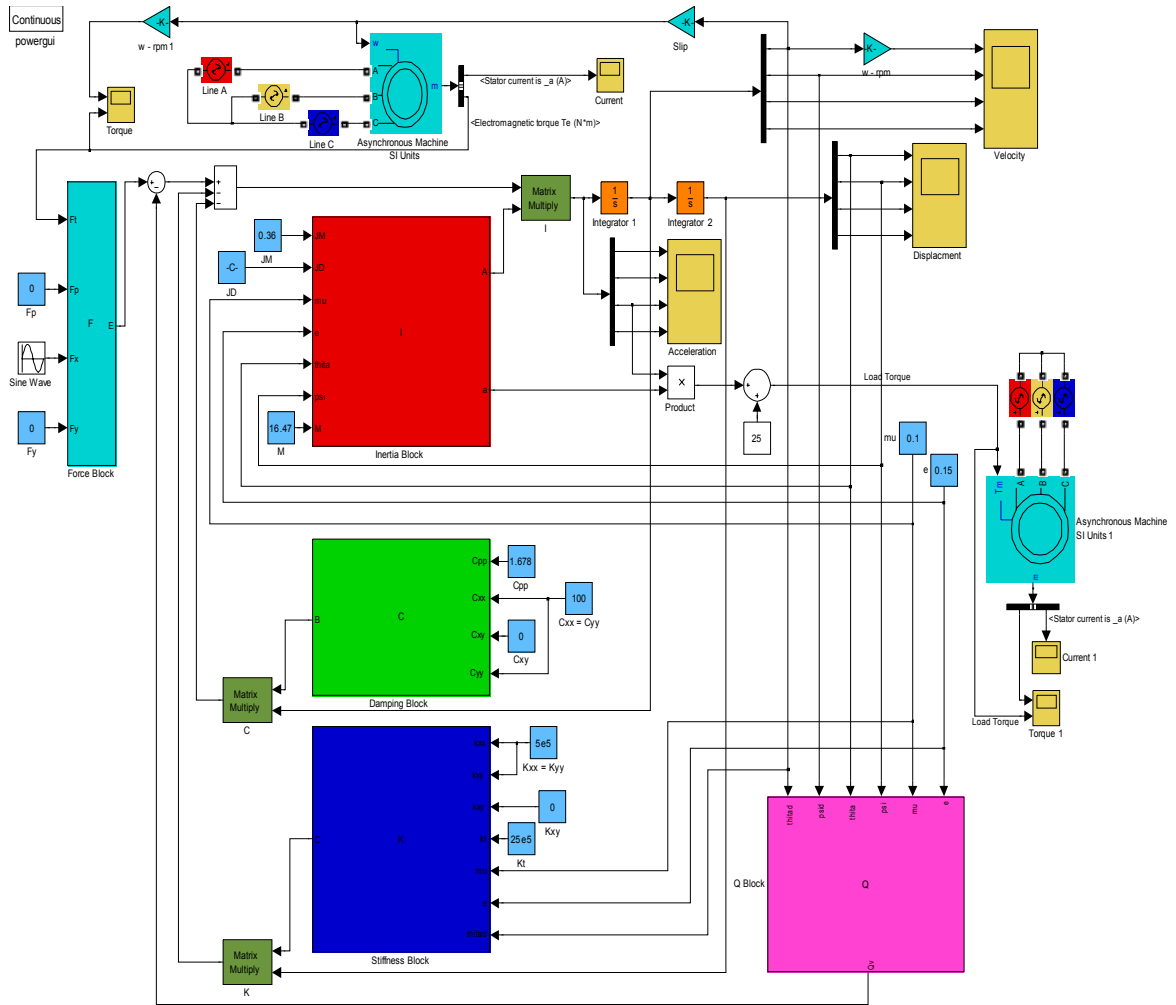


Figure 3.1.3: The Total System of the Coupled Motor Rotor.

One important thing worth mentioning is that the unbalance mass is set to be 0.1 kg to make significant effect on the motor current in the coupled system, where the misalignment sinusoidal force amplitude is set to be 100 N in X-axis direction.

3.2 Simulation Results

This section introduces the results obtained from running the simulation with the setup indicated in section 3.1 for the electrical system, mechanical system as well as the combined system.

3.2.1 Electrical System Simulation Results

The figures below show the results obtained by running the simulation for the electrical system only, the system is subjected to step applied three phase electrical power.

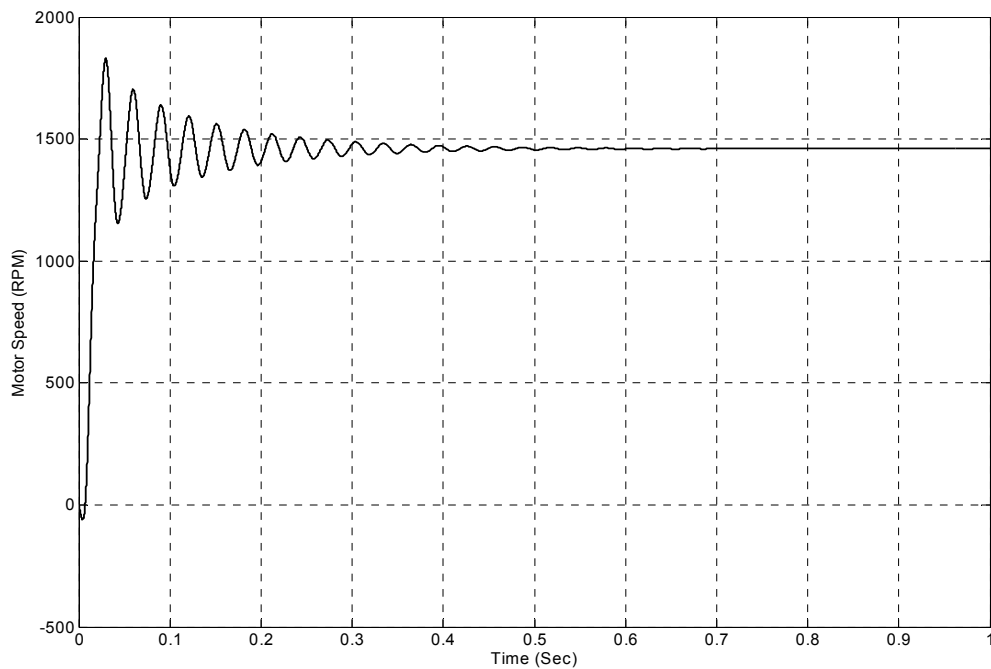


Figure 3.2.1: Induction Motor Speed in RPM.

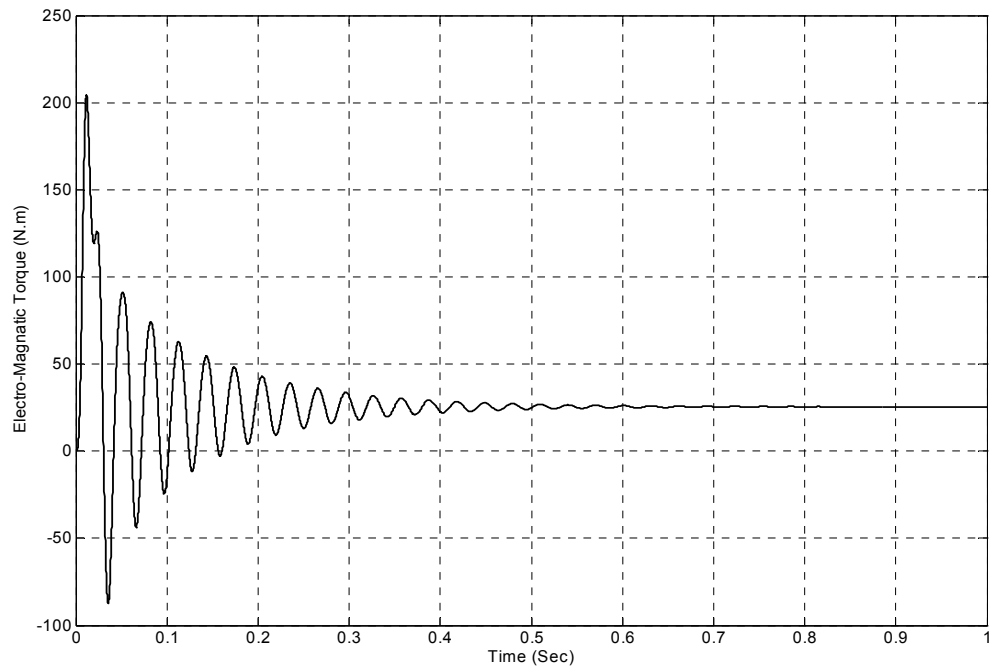


Figure 3.2.2: Induction Motor Electromagnetic Torque.

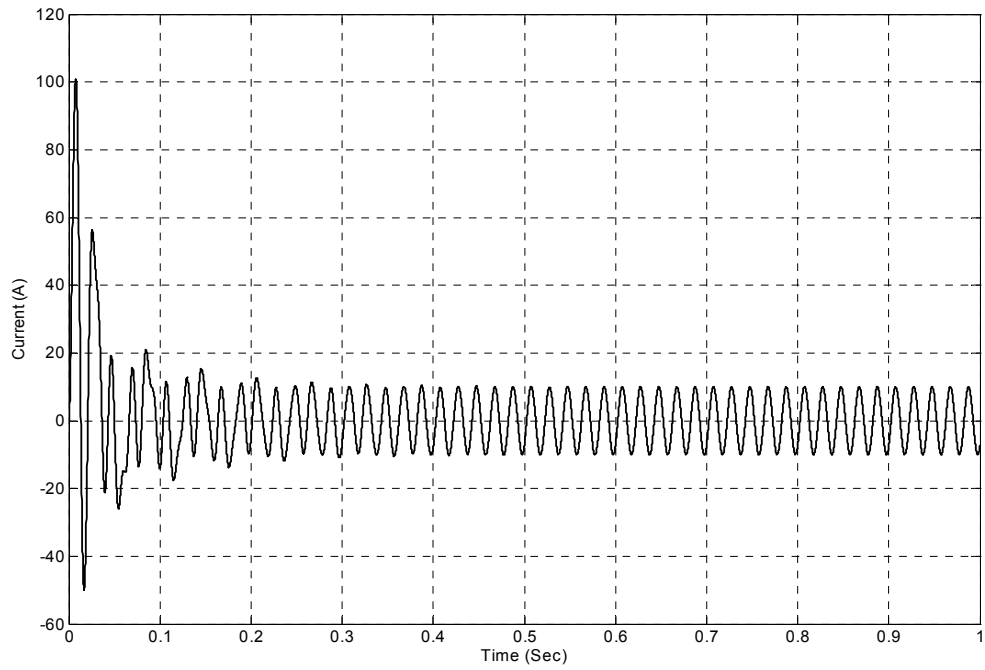


Figure 3.2.3: Induction Motor Stator Current.

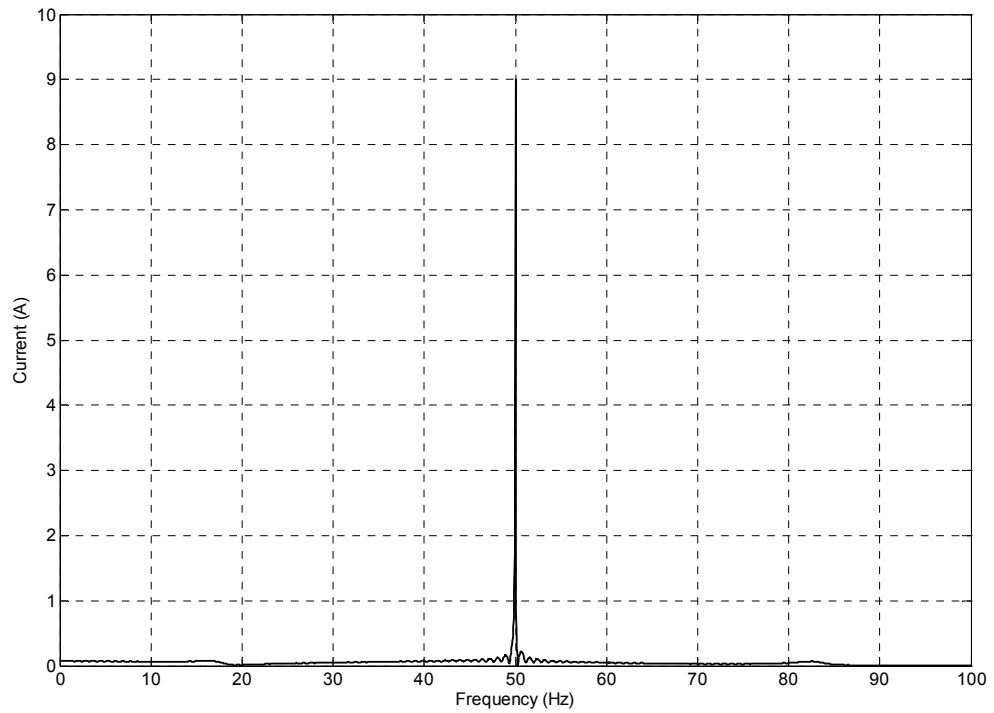


Figure 3.2.4: Stator Current Spectrum of Induction Motor Subjected to Constant Load Torque.

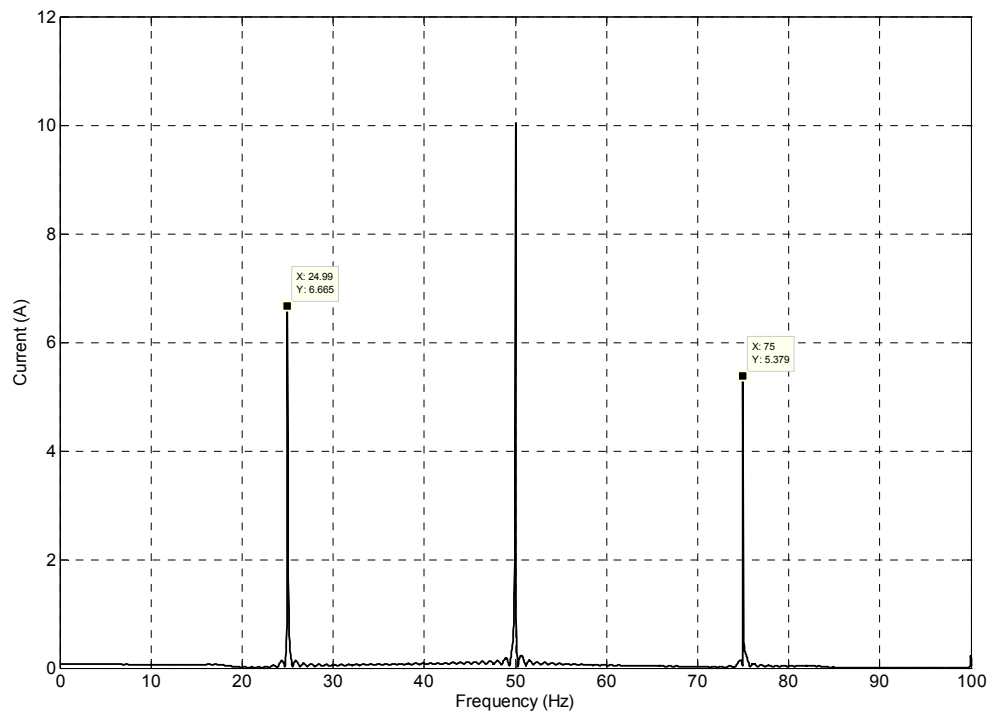


Figure 3.2.5: Stator Current Spectrum of Induction Motor Subjected to Sinusoidal Load Torque of Amplitude (25 N.m) with Frequency (25 Hz).

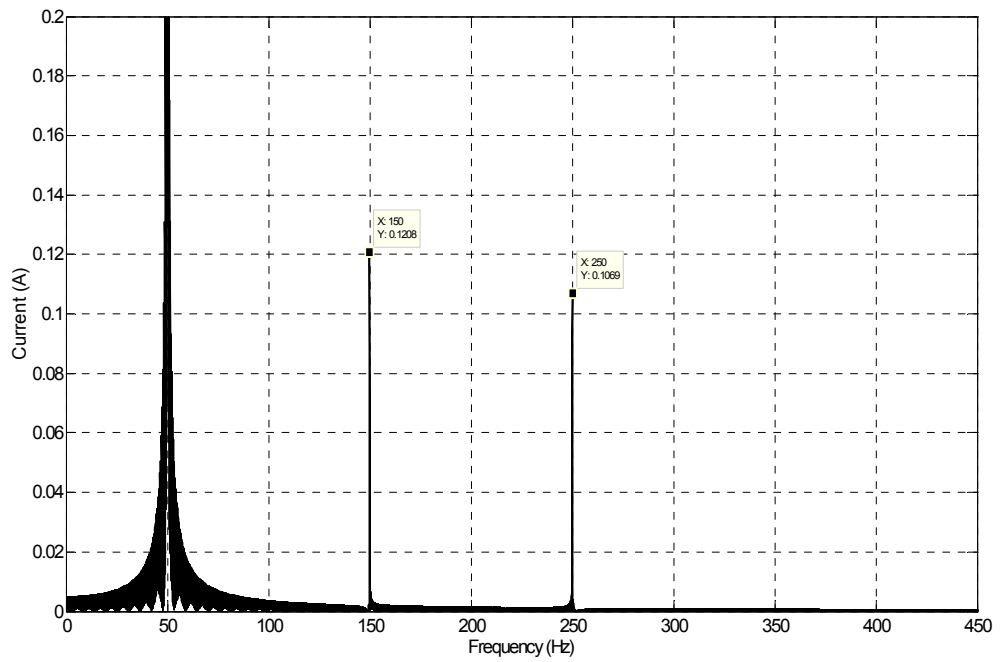


Figure 3.2.6a: Stator Current Spectrum of Induction Motor Subjected to Sinusoidal Load Torque of Amplitude (25 N.m) with Frequency (200 Hz).

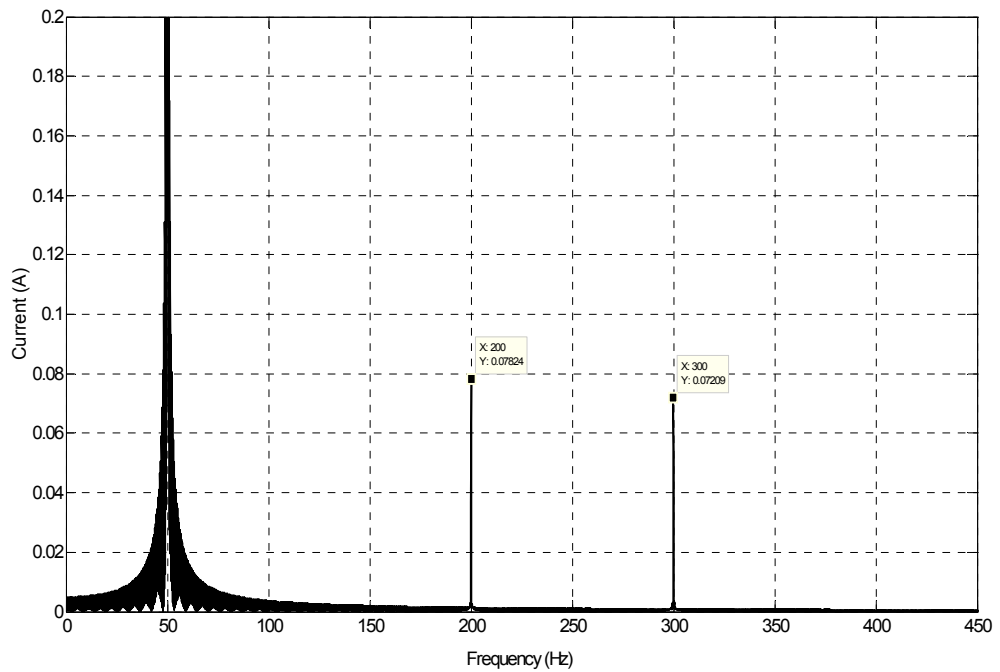


Figure 3.2.6b: Stator Current Spectrum of Induction Motor Subjected to Sinusoidal Load Torque of Amplitude (25 N.m) with Frequency (250 Hz).

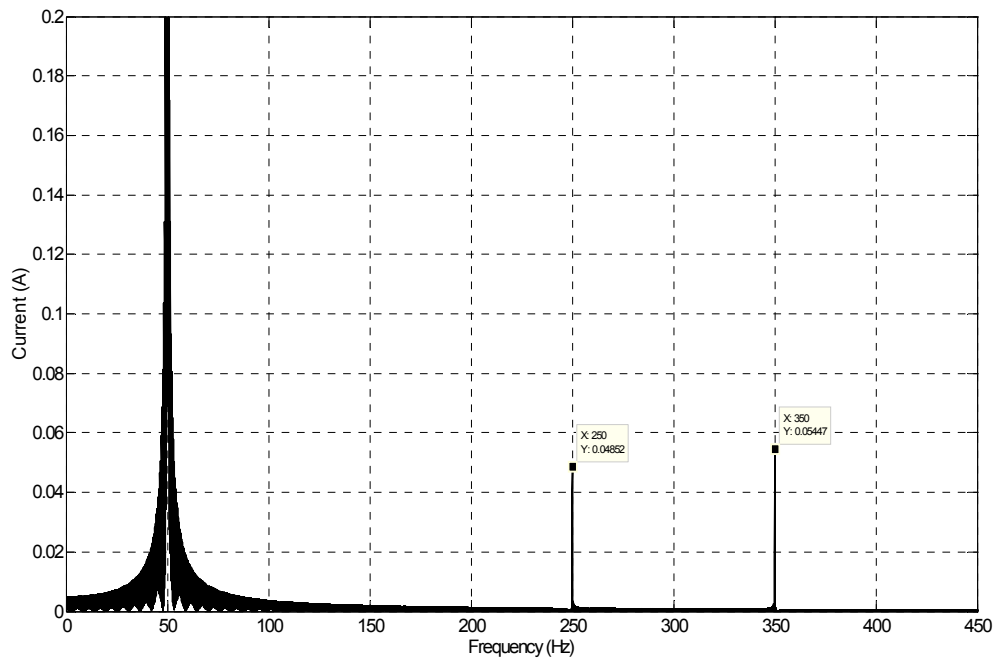


Figure 3.2.6c: Stator Current Spectrum of Induction Motor Subjected to Sinusoidal Load Torque of Amplitude (25 N.m) with Frequency (300 Hz).

3.2.2 Mechanical System Simulation Results

The figures below show the results obtained by running the simulation for the mechanical system only.

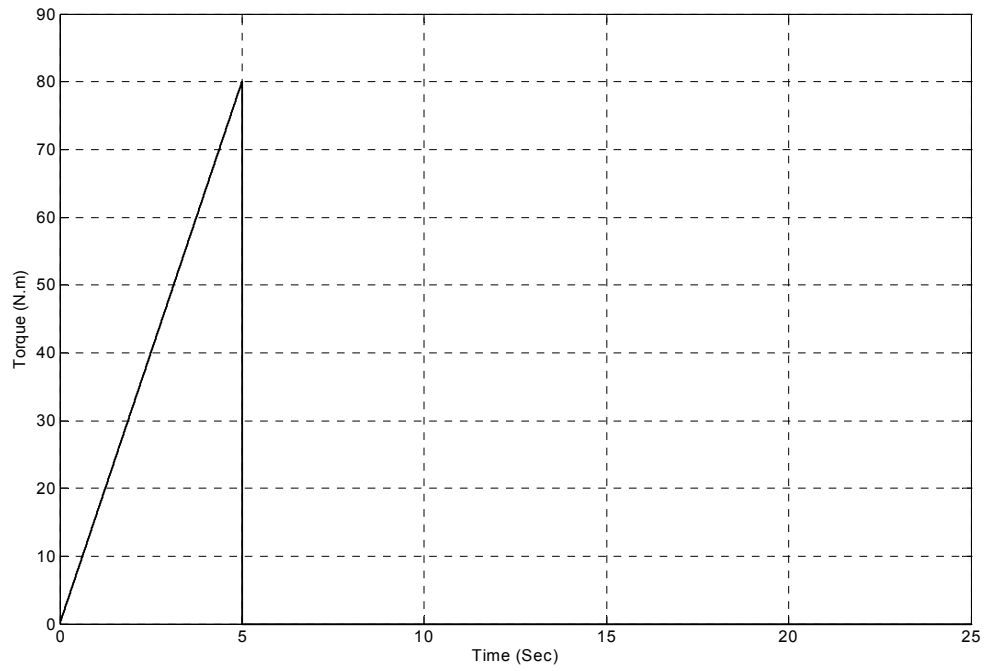


Figure 3.2.5: Rotor Input Torque.

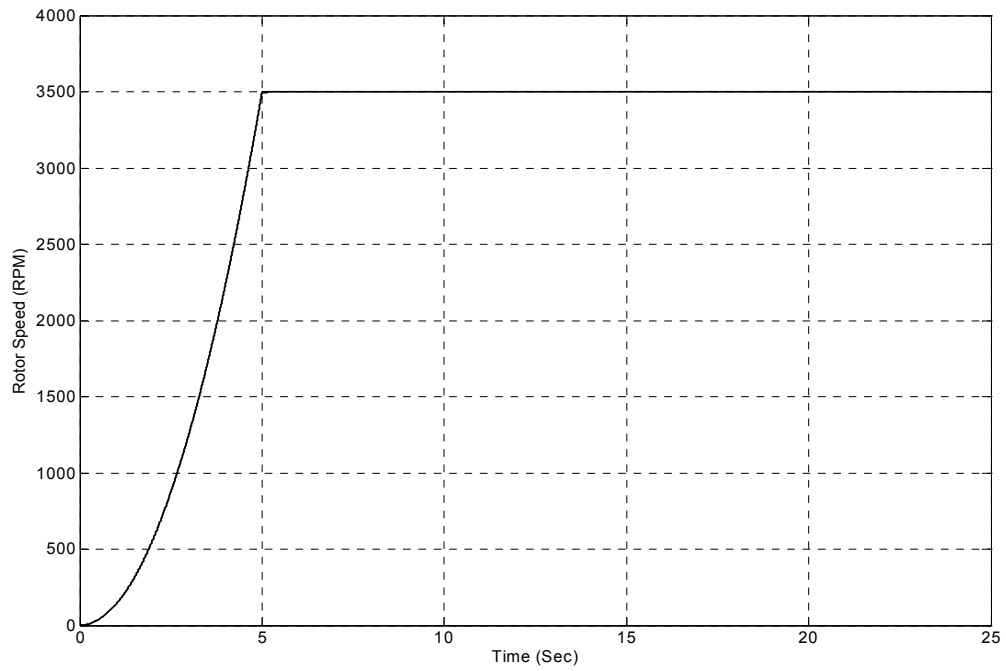


Figure 3.2.6: Rotor Speed in RPM.

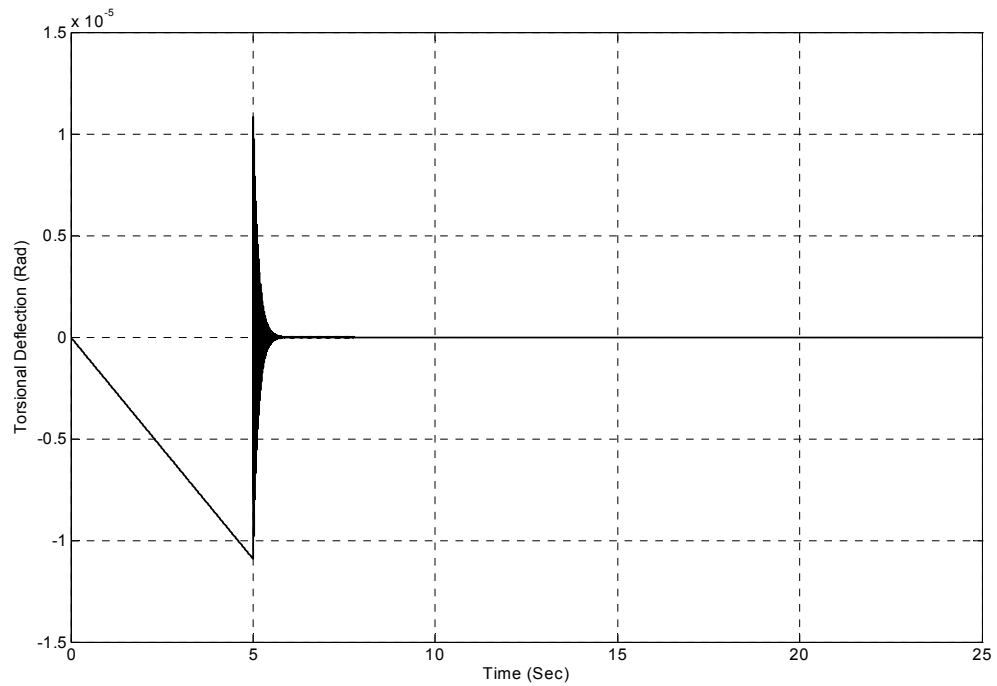


Figure 3.2.7: Rotor Torsional Deflection.

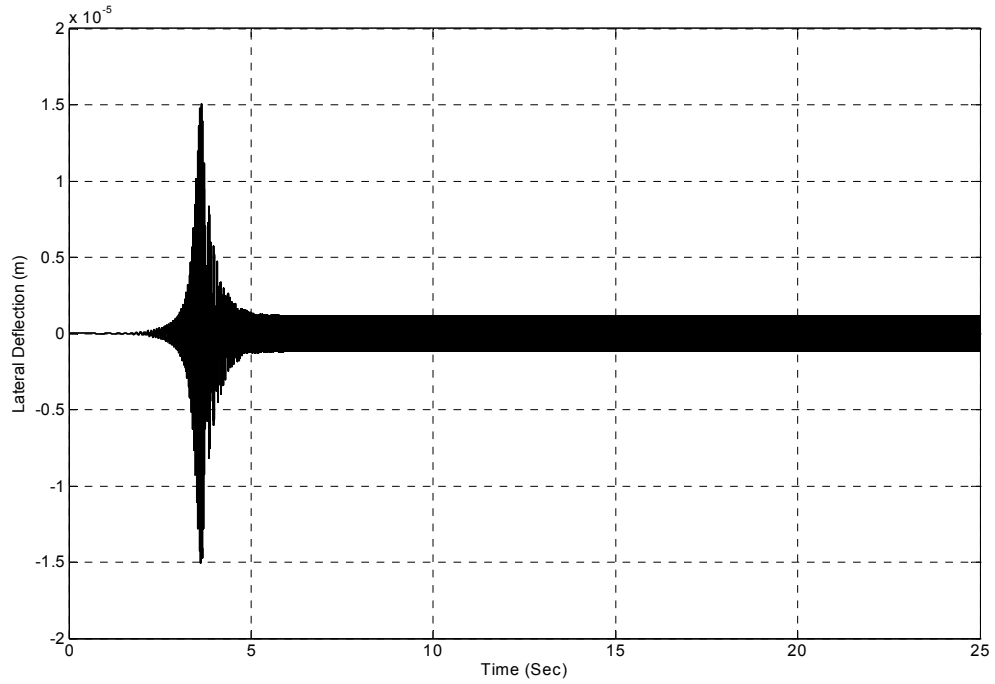


Figure 3.2.8: Rotor Lateral Deflection.

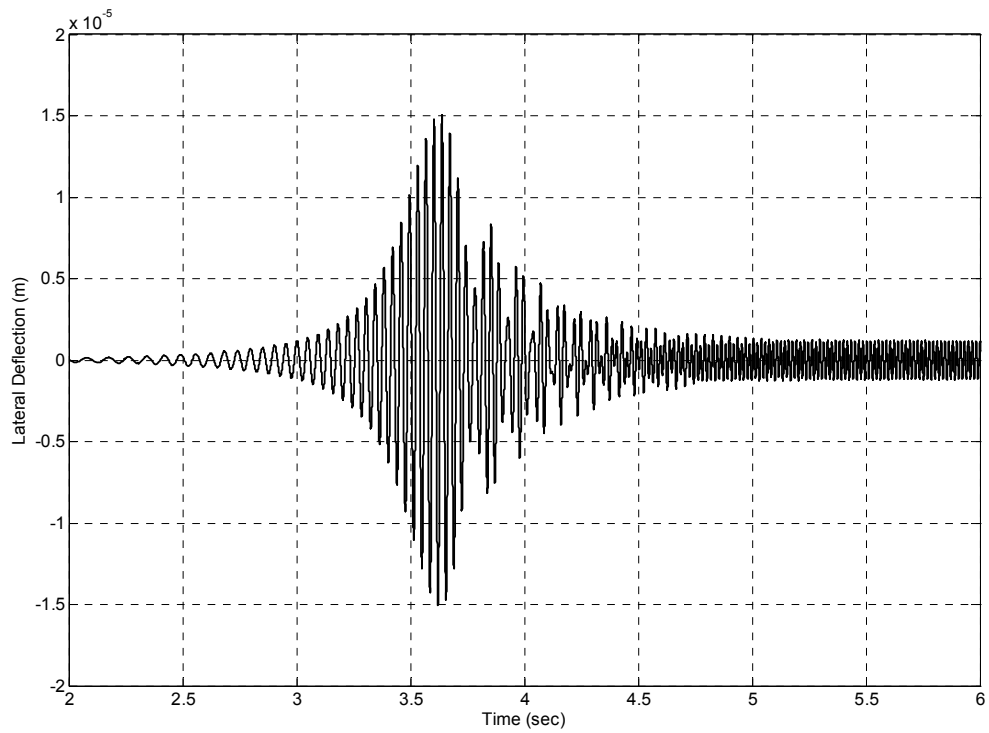


Figure 3.2.8a: Rotor Lateral Deflection (Zoomed View).

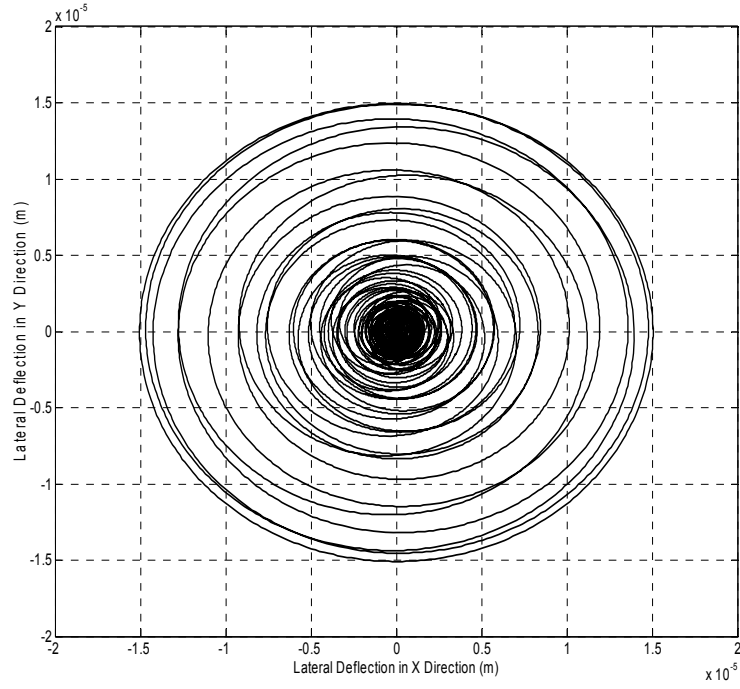


Figure 3.2.9: Rotor Lateral Deflection in XY Plane.

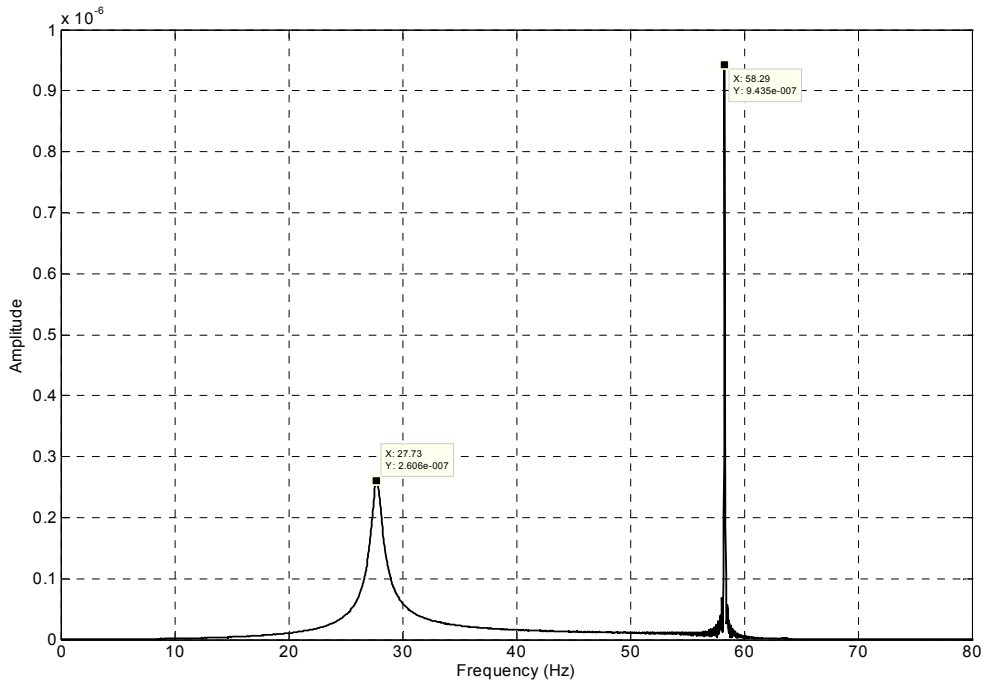


Figure 3.2.10: Rotor Lateral Deflection Frequency Spectrum.

3.2.3 Combined System Simulation Results

This section presents the results obtained by running the simulation for the combined system (mechanical and electrical). A total of three *main* figure groups are displayed. Initially, a spectrum of the healthy motor is shown for comparison purposes, then one group of figures will indicate the unbalance, and finally the second group will contain the unbalance *and* misalignment figures.

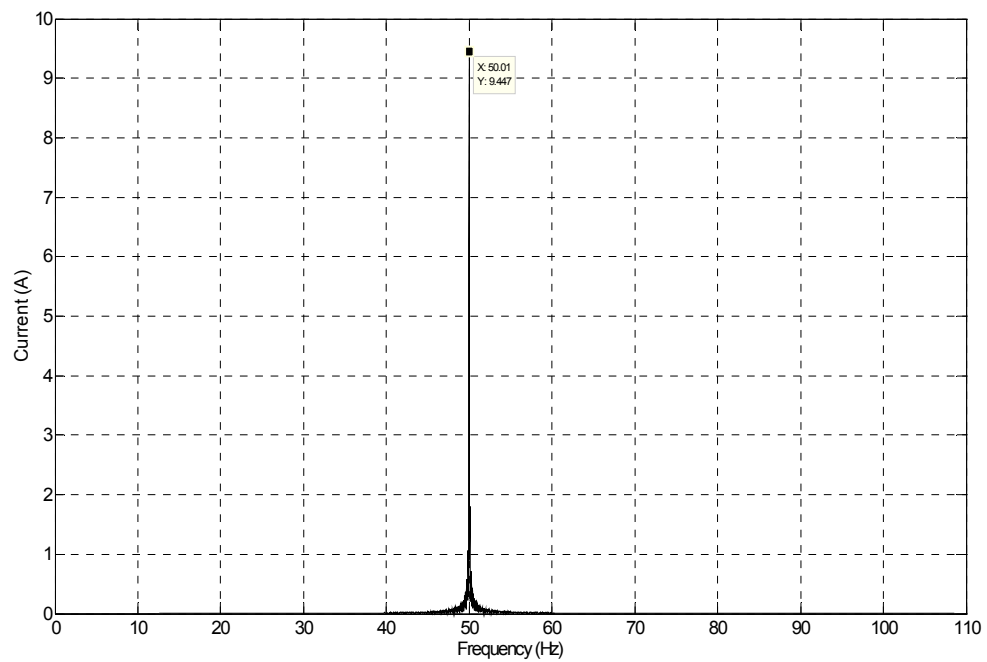


Figure 3.2.11: Motor Current Frequency Spectrum for Healthy Rotor.

3.2.3.1 Unbalanced Rotor Results

This section presents the results obtained by running the simulation simultaneously for the mechanical behavior of the system, i.e. the vibration amplitude against time and for both directions x and y, and also for the motor current signature.

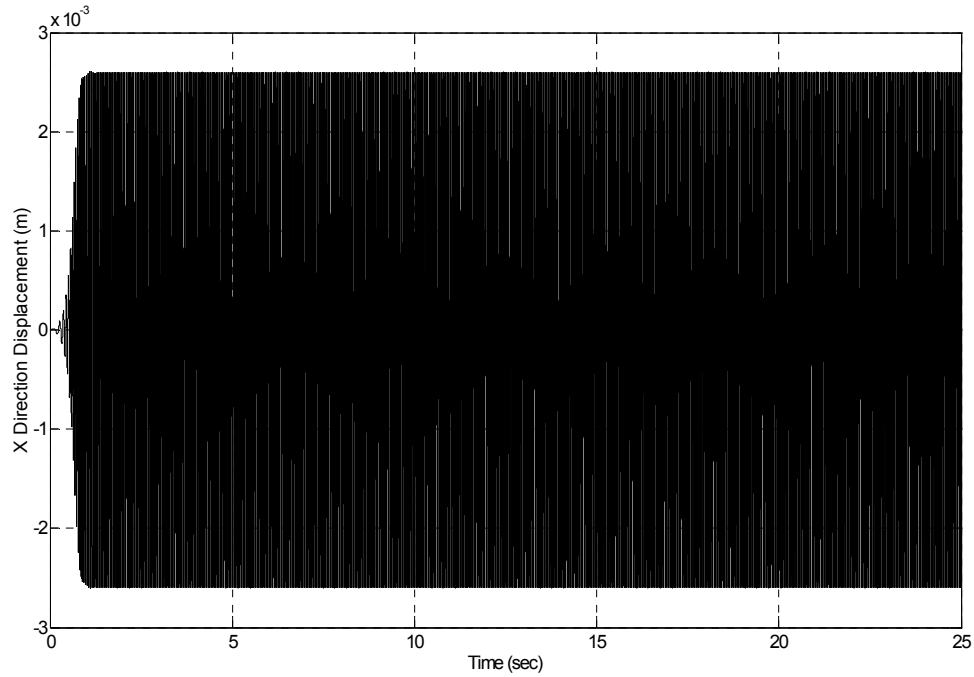


Figure 3.2.12: Unbalanced Rotor Displacement in X Direction vs. Time.

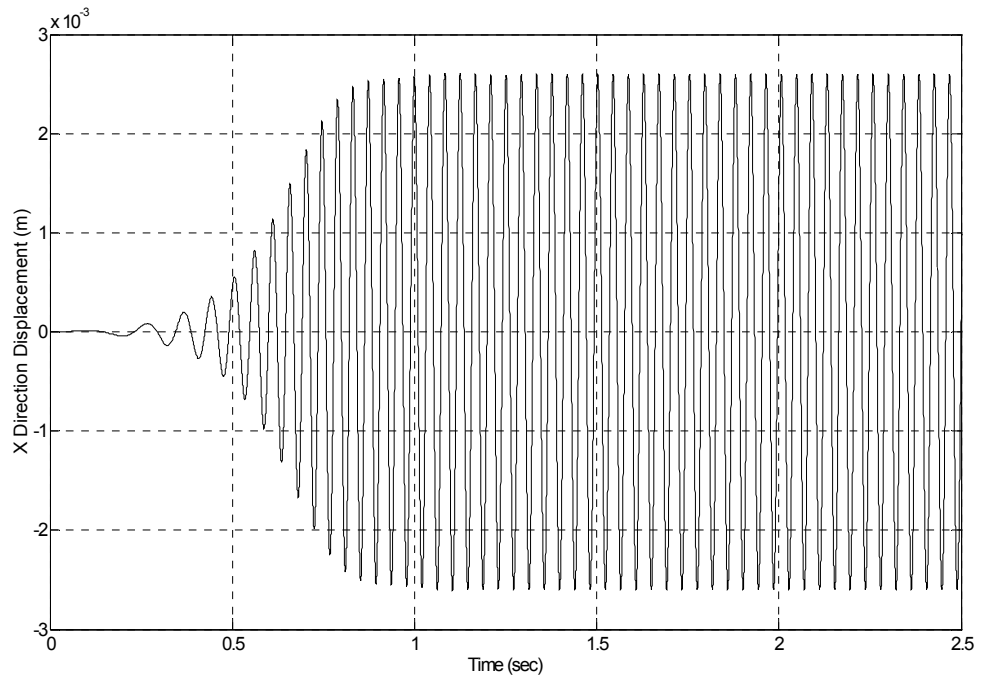


Figure 3.2.12a: Unbalanced Rotor Displacement in X Direction vs. Time (Zoomed View).

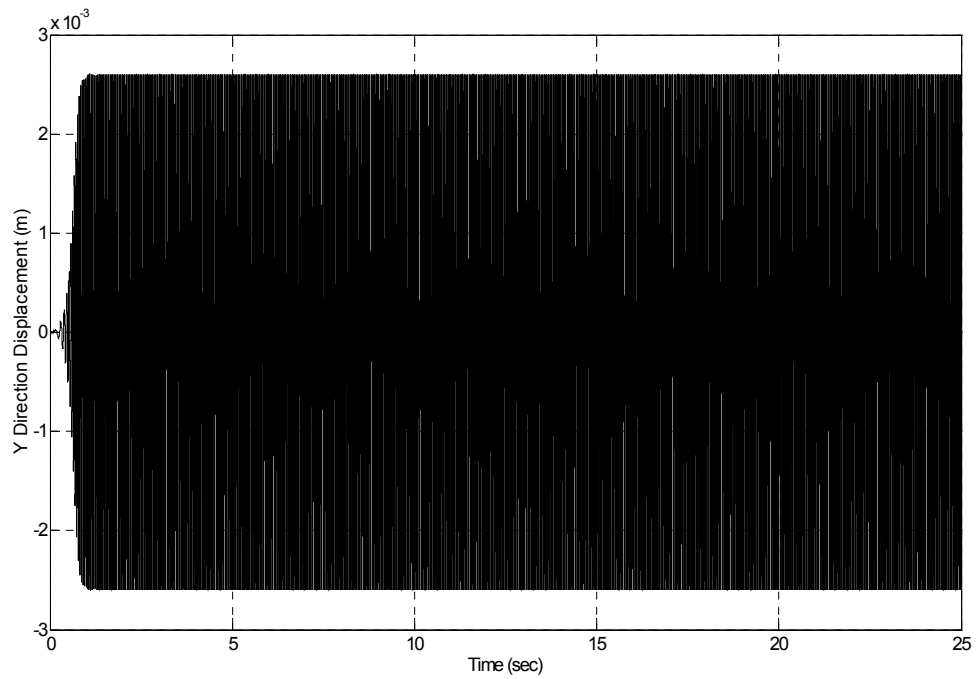


Figure 3.2.13: Unbalanced Rotor Displacement in Y Direction vs. Time.

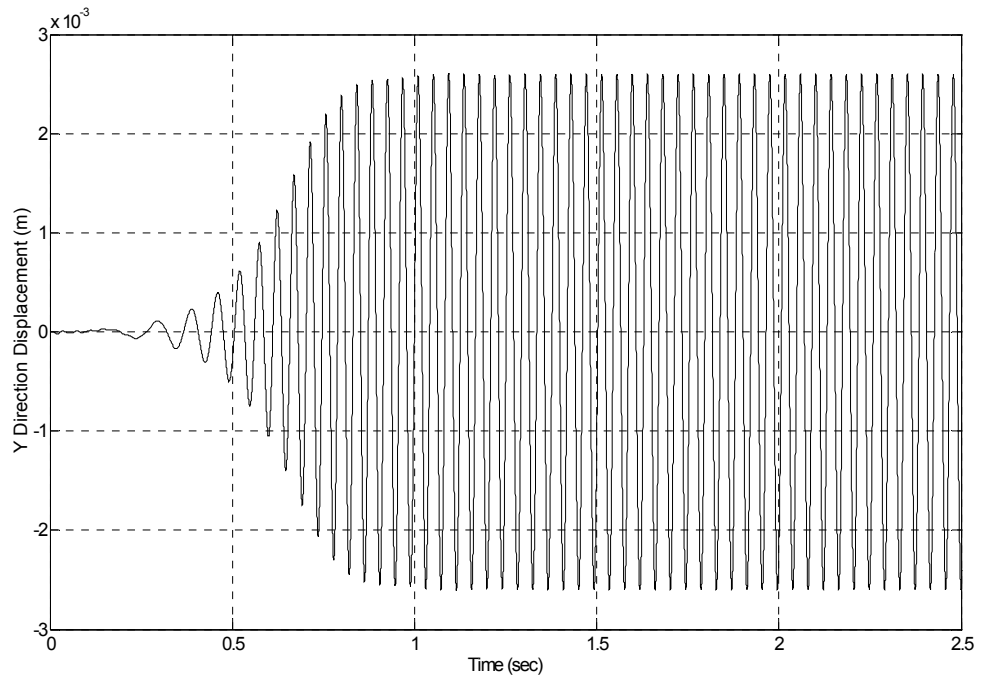


Figure 3.2.13a: Unbalanced Rotor Displacement in Y Direction vs. Time (Zoomed View).

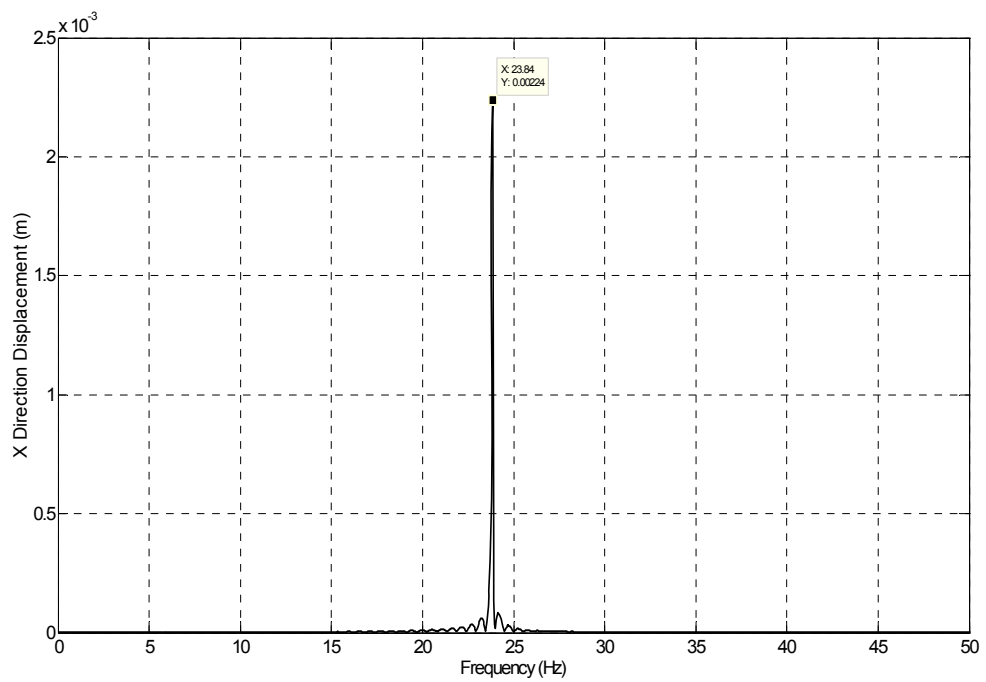


Figure 3.2.14: Unbalanced Rotor Displacement in X Direction Spectrum

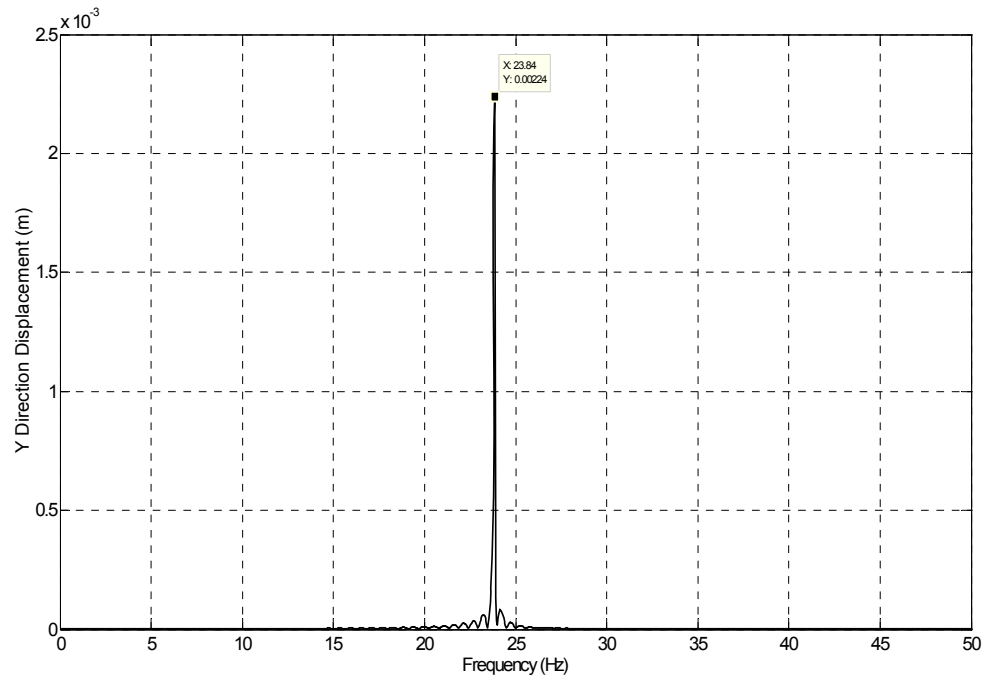


Figure 3.2.15: Unbalanced Rotor Displacement in Y Direction Spectrum

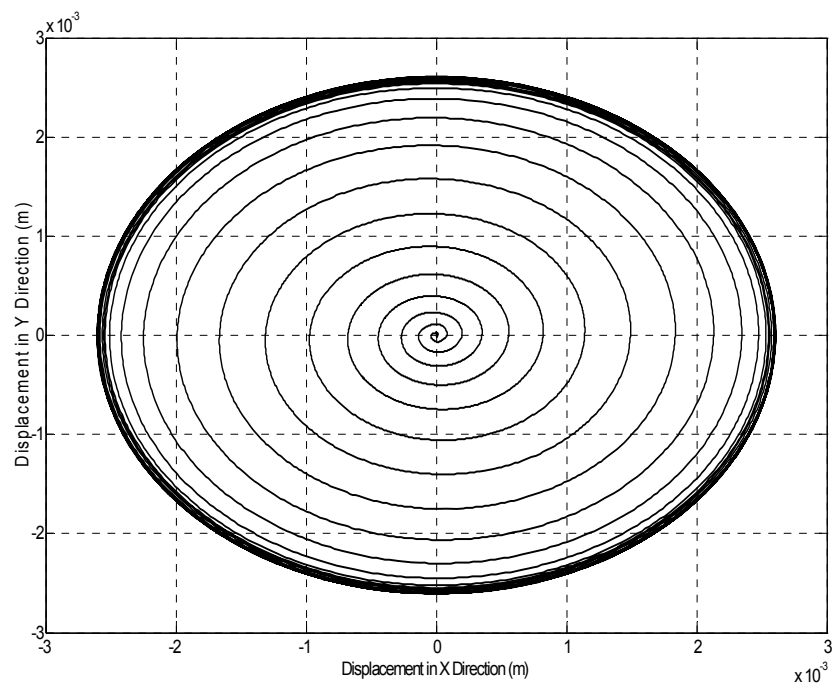


Figure 3.2.16: Unbalanced Rotor Displacement in XY Plain.

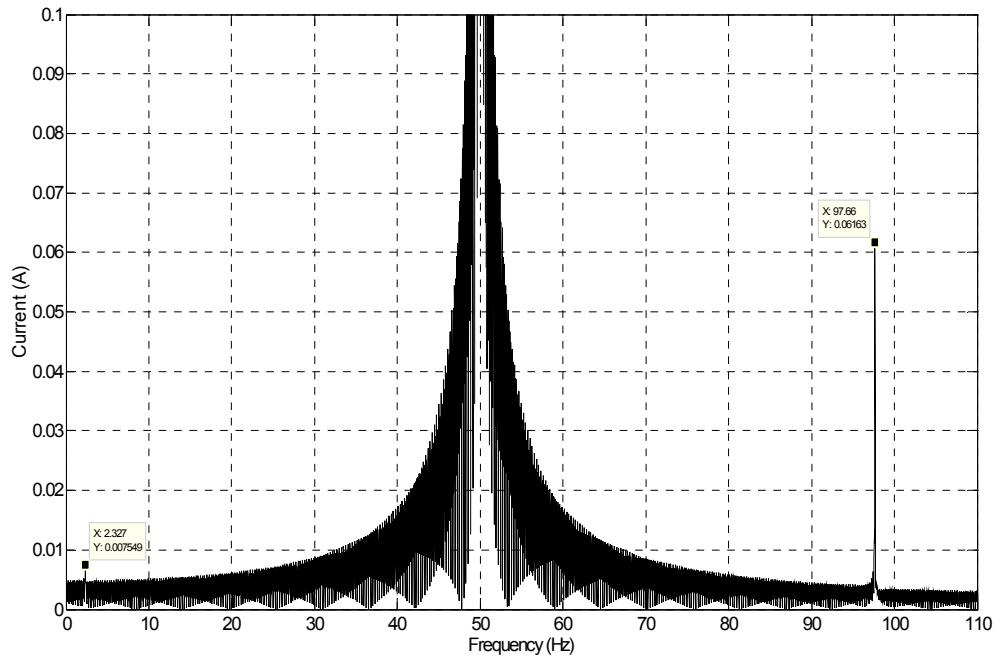


Figure 3.2.17: Motor Stator Current Spectrum for Unbalanced Rotor.

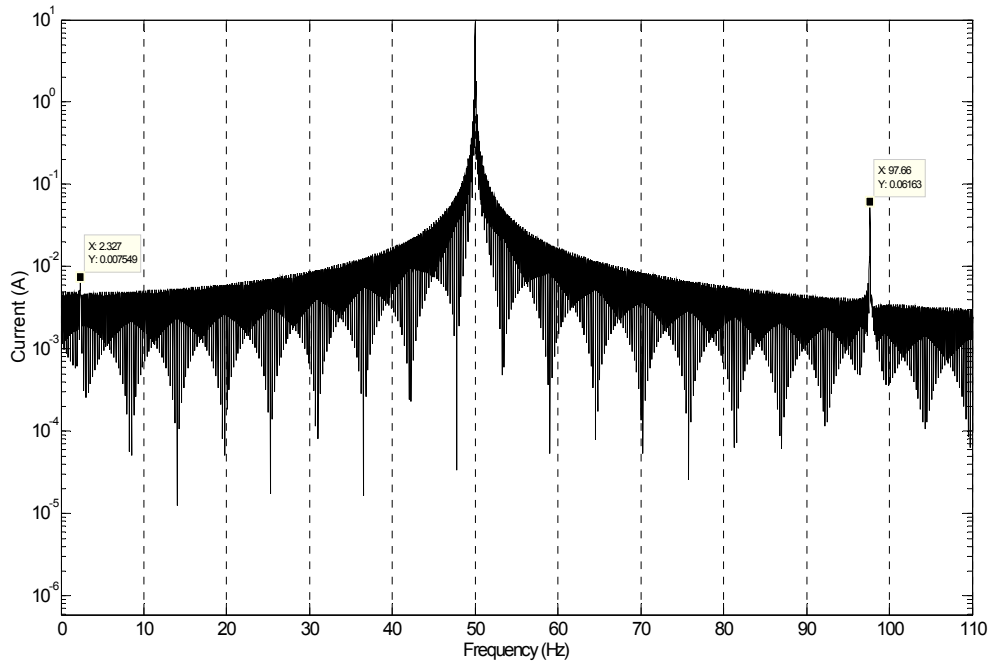


Figure 3.2.18: Motor Stator Current Spectrum for Unbalanced Rotor in Logarithmic Scale.

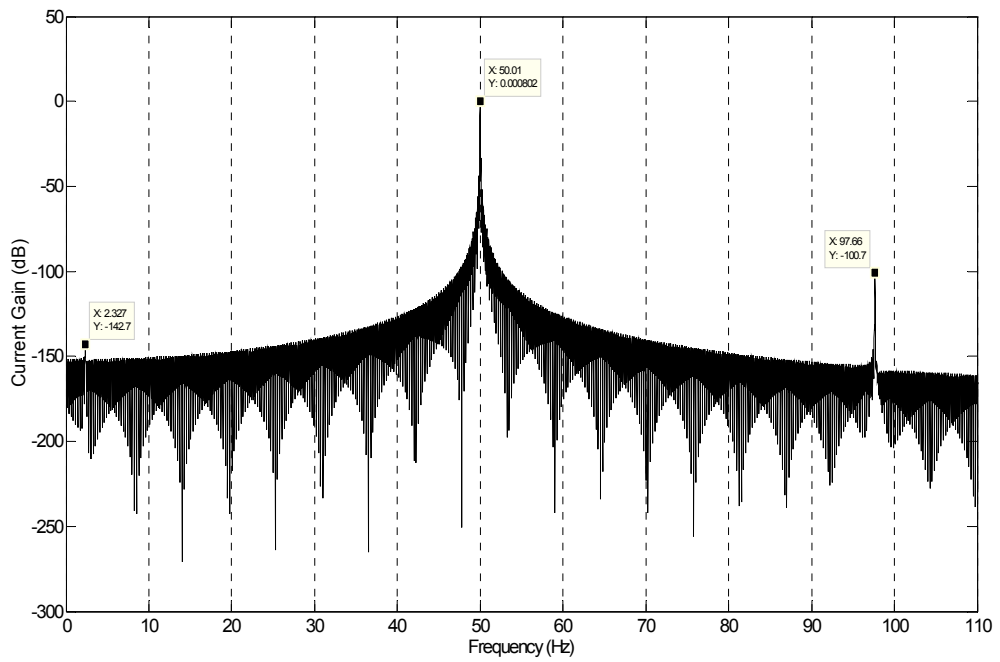


Figure 3.2.19: Motor Stator Current Gain Spectrum for Unbalanced Rotor.

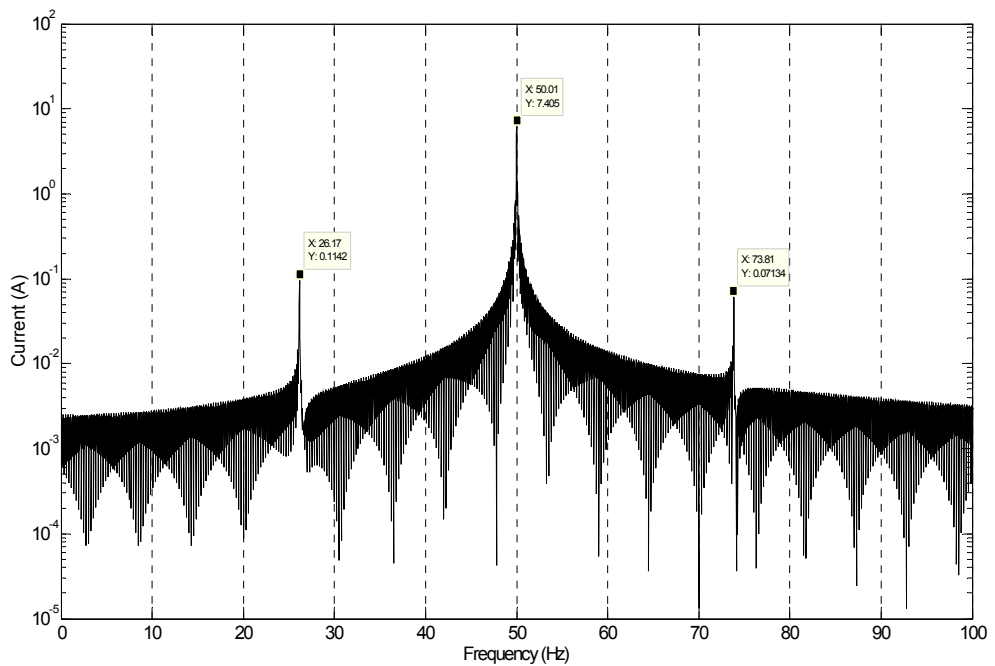


Figure 3.2.20: Stator Current Spectrum for 8 Poles Induction Motor (715 RPM) with Unbalanced Rotor.

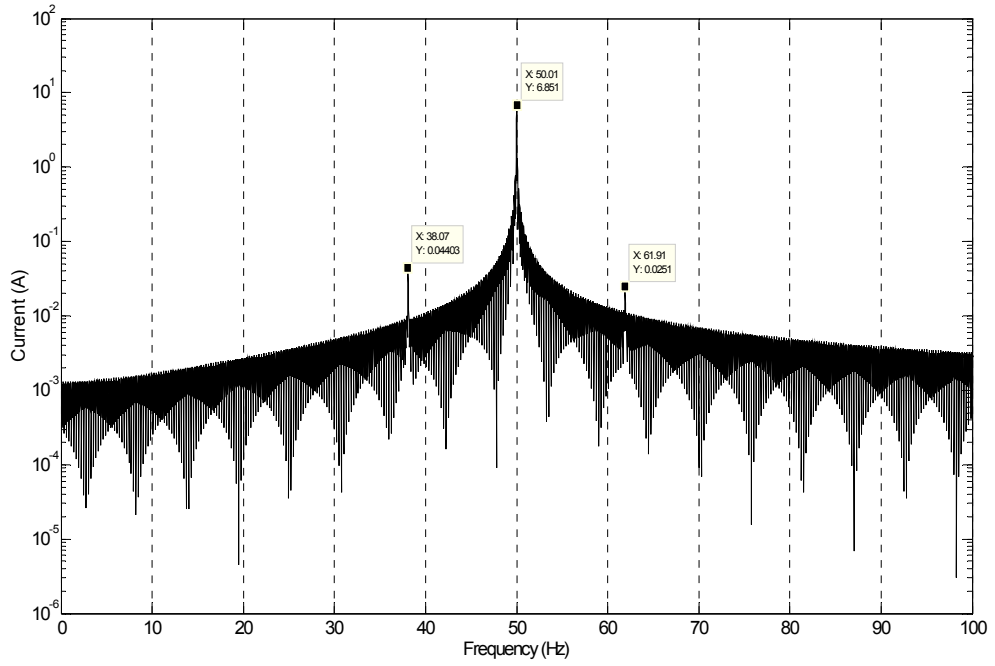


Figure 3.2.21: Stator Current Spectrum for 16 Poles Induction Motor (357.5 RPM) with Unbalanced Rotor.

3.2.3.2 Unbalanced and Misaligned Rotor Results

This section presents the results obtained by running the simulation simultaneously for the mechanical behavior of the system, i.e. the vibration amplitude against time and for both directions x and y , and also for the motor current signature for the case of misaligned and unbalanced rotor. The importance of combining the misalignment and unbalance is that the mathematical model will yield trivial results if the unbalance effects were set to zero. In addition, realistic applications never have perfectly balanced rotors. This is the intuitive step after having studied the effects of unbalance on its own, so they can be easily isolated from the case of misalignment when the combined effects are present.

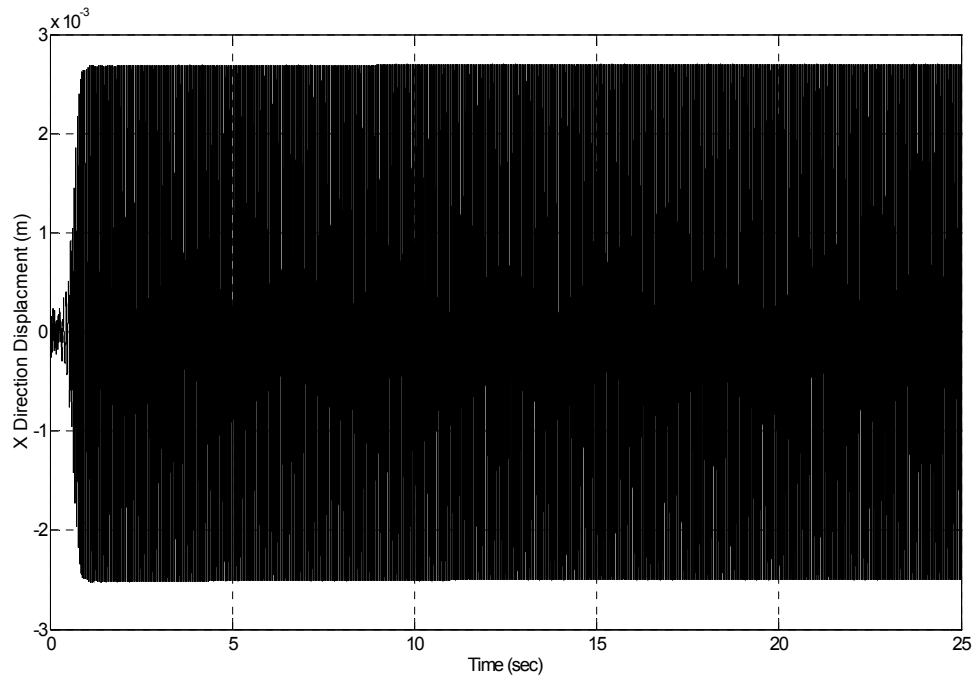


Figure 3.2.22: Unbalanced and Misaligned Rotor Displacement in X Direction vs. Time.

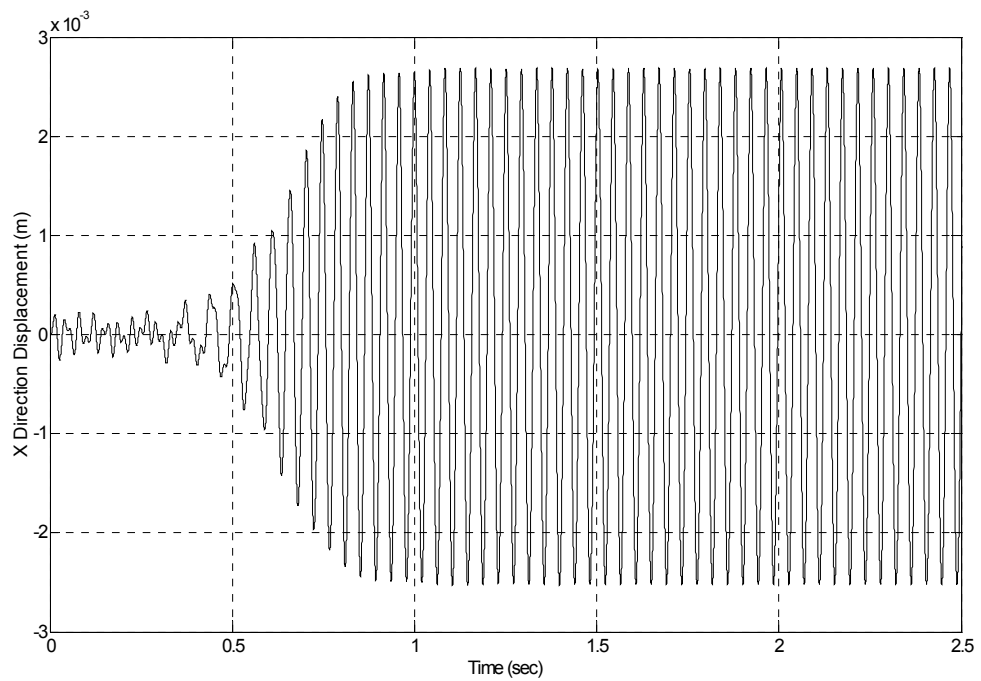


Figure 3.2.22a: Unbalanced and Misaligned Rotor Displacement in X Direction vs. Time (Zoomed View).

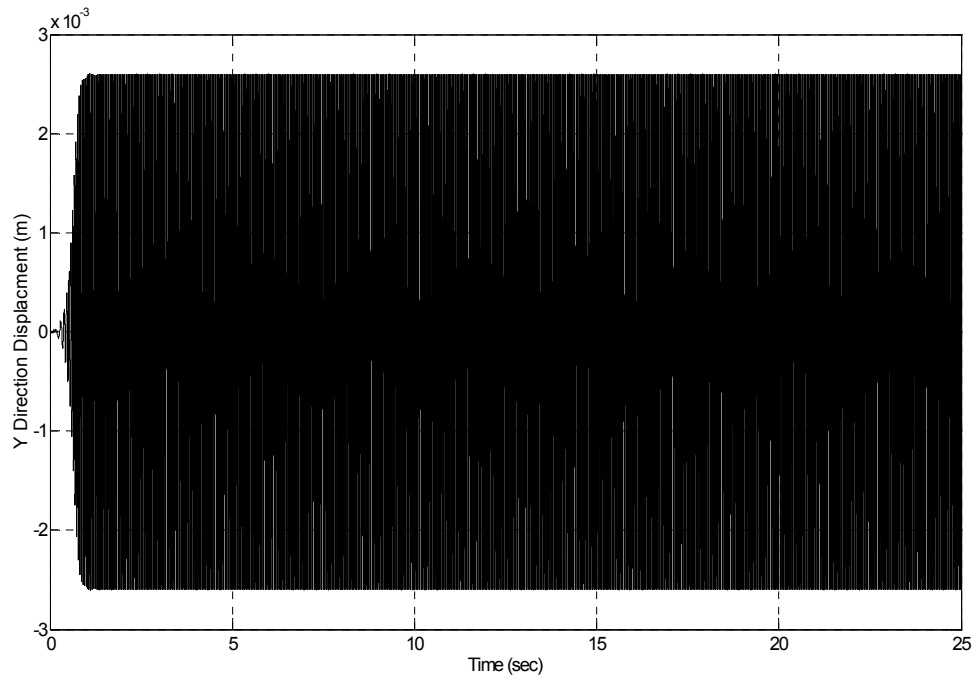


Figure 3.2.23: Unbalanced and Misaligned Rotor Displacement in Y Direction vs. Time.

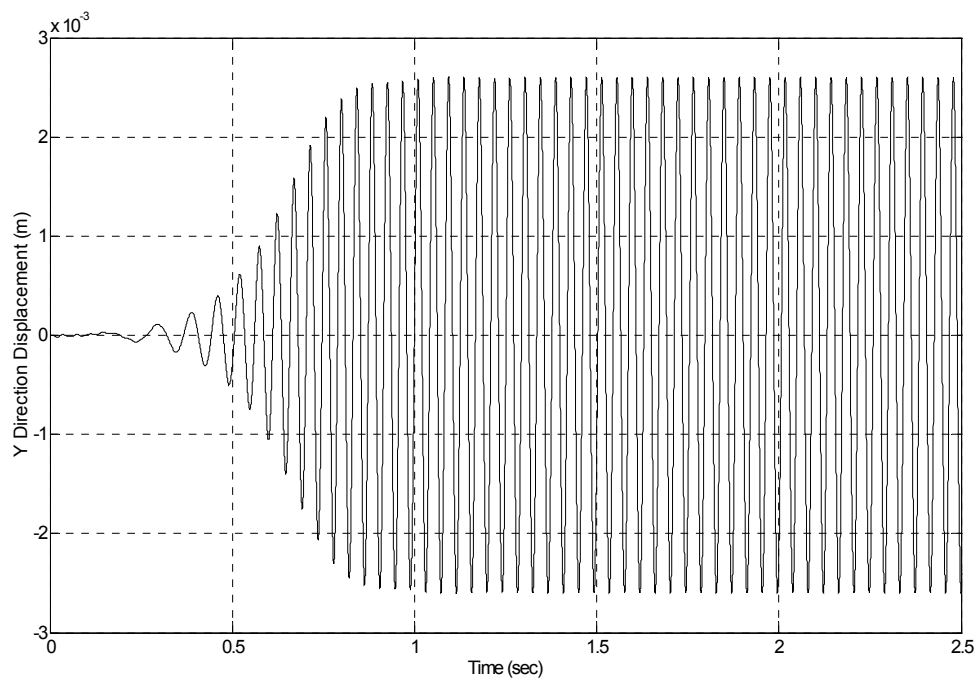


Figure 3.2.23a: Unbalanced and Misaligned Rotor Displacement in Y Direction vs. Time (Zoomed View).

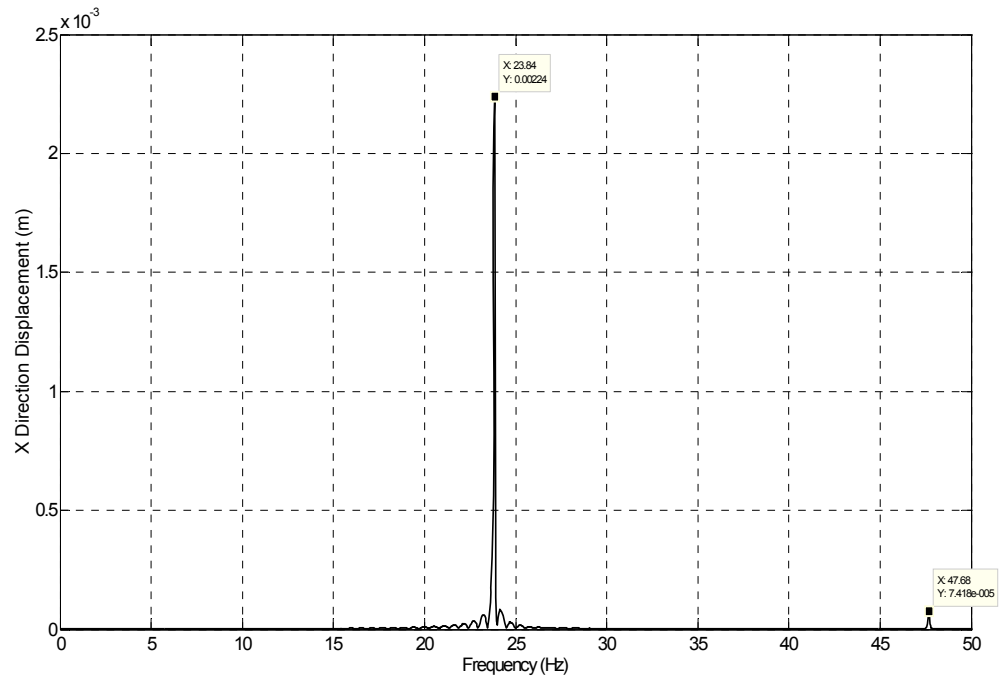


Figure 3.2.24: Unbalanced and Misaligned Rotor Displacement in X Direction Spectrum.

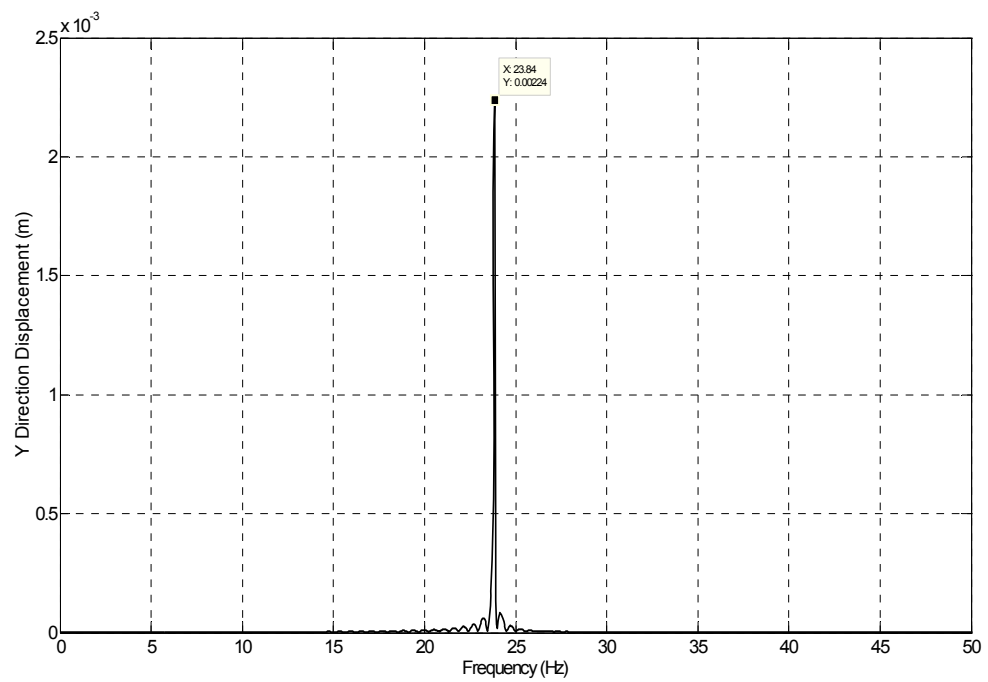


Figure 3.2.25: Unbalanced and Misaligned Rotor Displacement in Y Direction Spectrum.

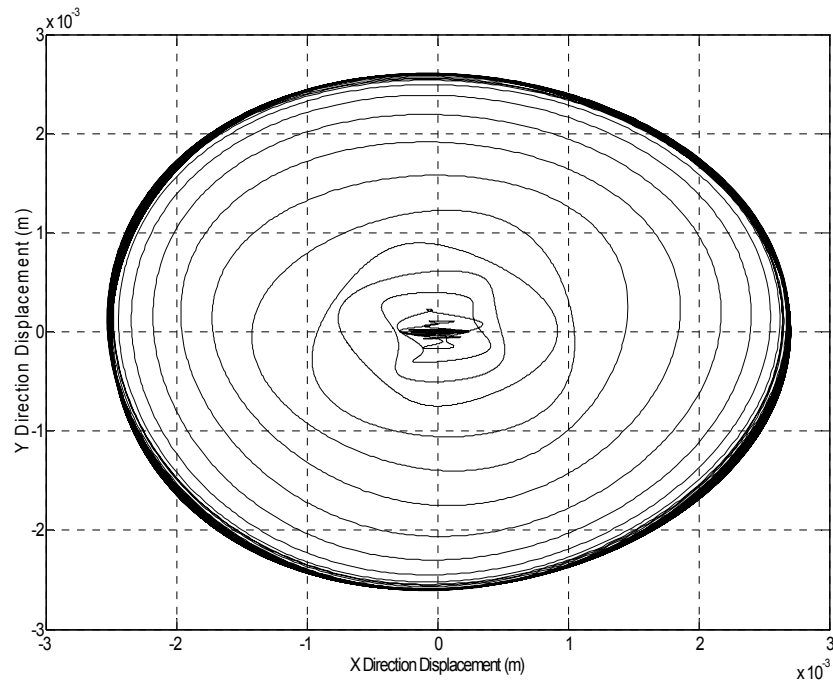


Figure 3.2.26: Unbalanced and Misaligned Rotor Displacement in XY Plain.

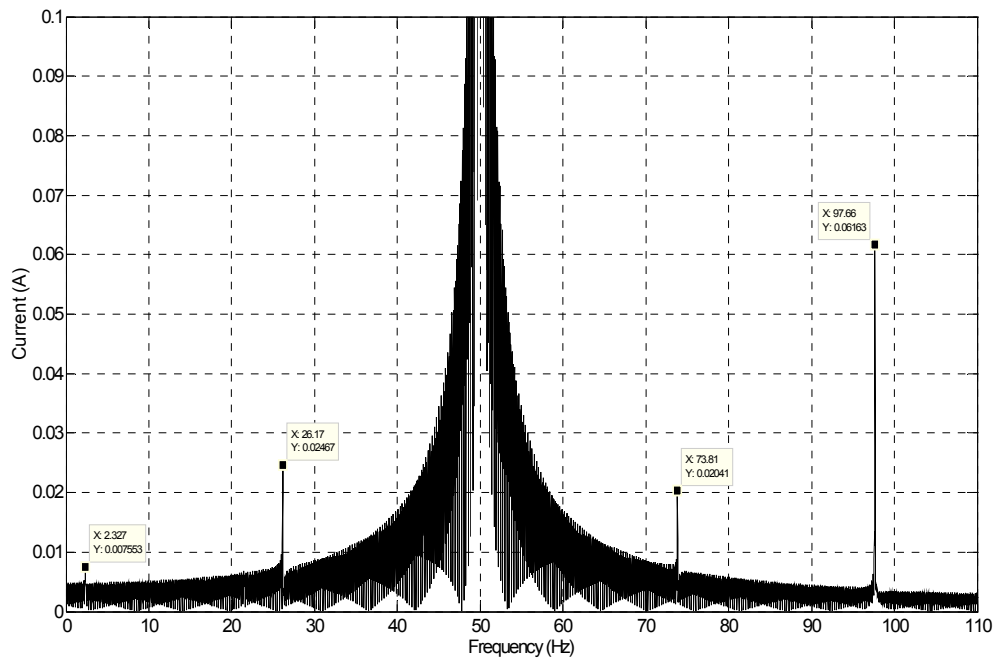


Figure 3.2.27: Motor Stator Current Spectrum for Unbalanced and Misaligned Rotor.

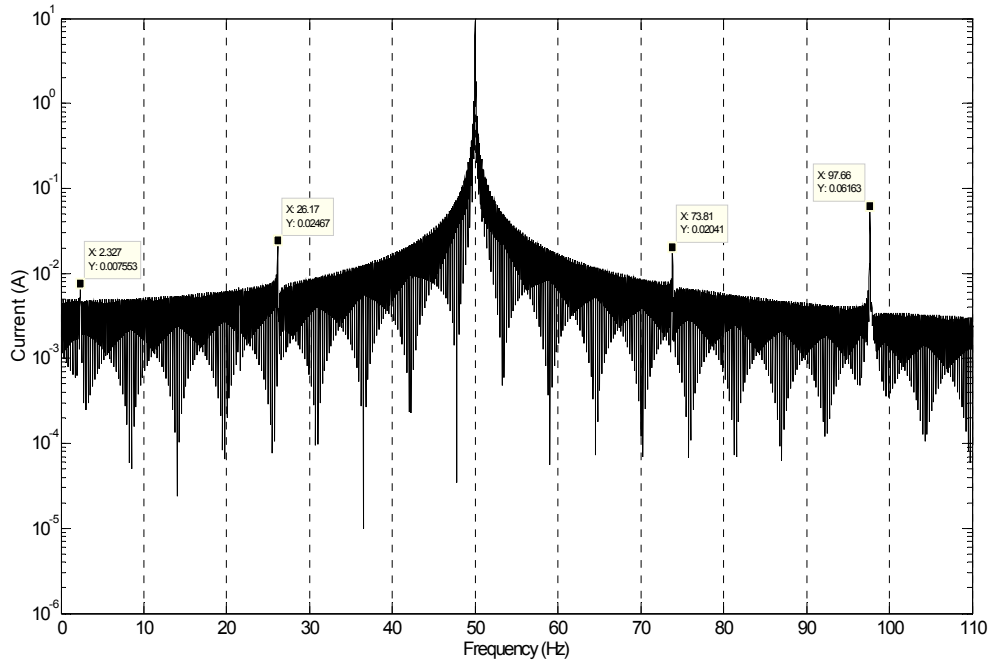


Figure 3.2.28: Motor Stator Current Spectrum for Unbalanced and Misaligned Rotor in Logarithmic Scale.

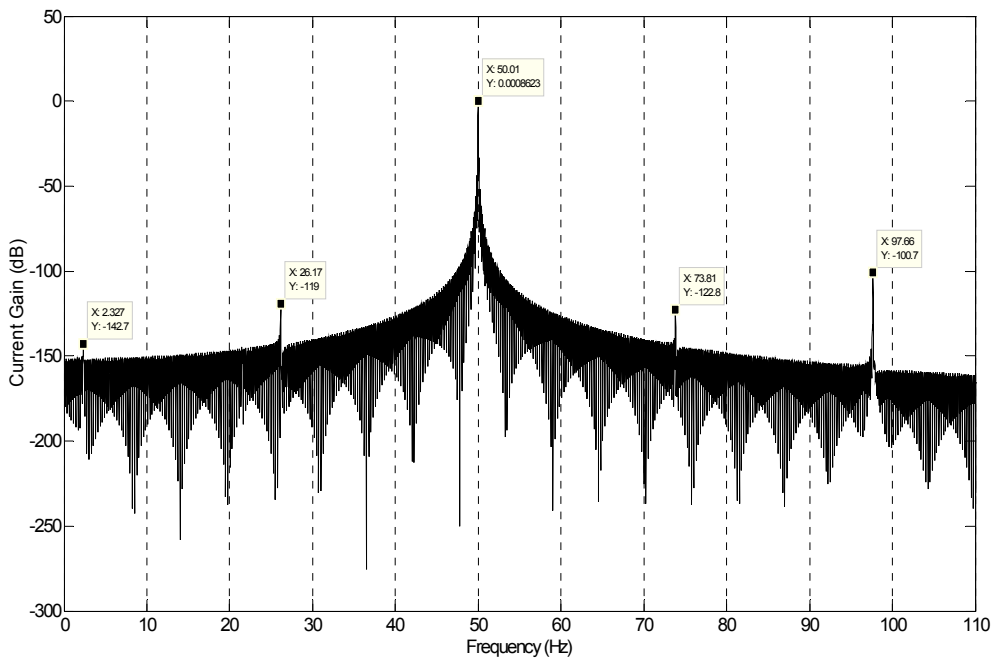


Figure 3.2.29: Motor Stator Current Gain Spectrum for Unbalanced and Misaligned Rotor.

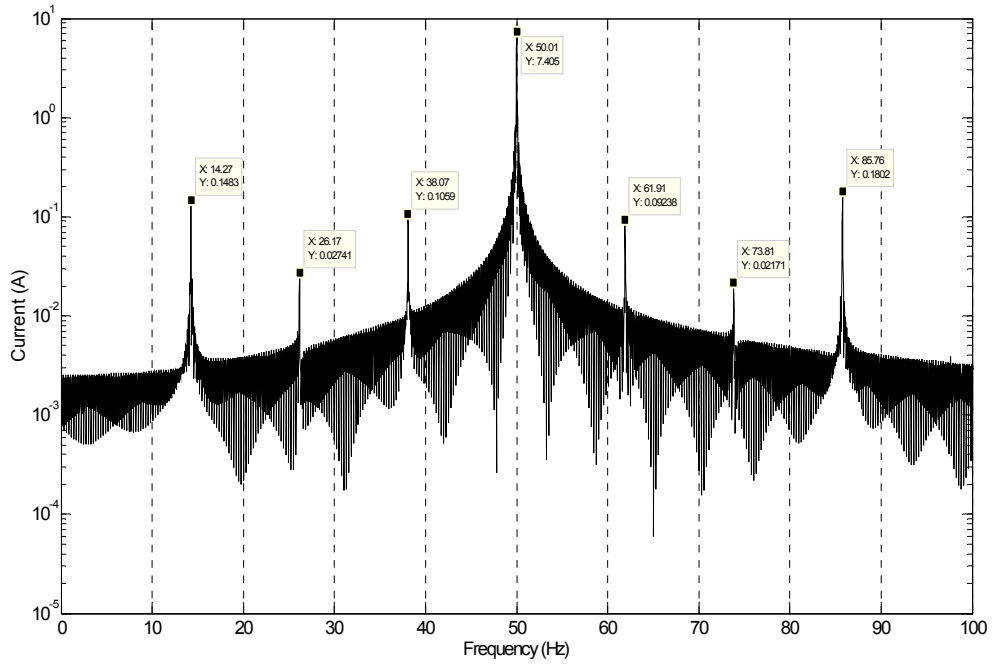


Figure 3.2.30: Stator Current Spectrum for 8 Poles Induction Motor (715 RPM) with Unbalanced and Misaligned Rotor.

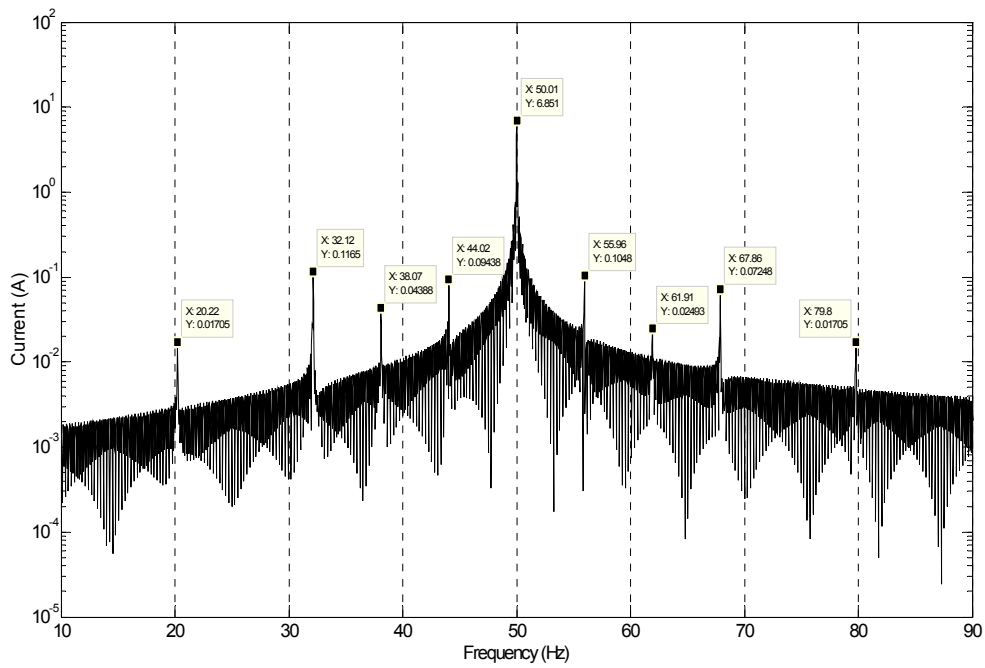


Figure 3.2.31: Stator Current Spectrum for 16 Poles Induction Motor (357.5 RPM) with Unbalanced and Misaligned Rotor.

3.3 Parametric Study of Unbalance Mass and Misalignment Force

This parametric study will help in better understanding the relationship between the unbalance and misalignment of the rotor and how the change in one affects the other. Table (3.3.1) below shows different mass unbalance values with the corresponding values of high frequency spectra amplitude to be plotted and compared for the constant misalignment case. Table (3.3.2) relates the changing values of the misalignment force versus the values high frequency spectra.

The plot of the data in tables (3.3.1) and (3.3.2) are shown in figures (3.3.1) and (3.3.2) respectively.

Table 3.3.1: Values of Motor Current Spectra with Mass Unbalance.

Mass unbalance (kg)	Spectra Amplitude (A)
0.00	0.00000
0.05	0.01458
0.10	0.05945
0.15	0.13690
0.20	0.22210
0.25	0.27050
0.30	0.53780
0.35	0.16160
0.40	0.95230

Table 3.3.2: Values of Motor Current Spectra with Rotor Misalignment.

Misalignment Force (N)	Spectra Amplitude (A)
0	0.00000
50	0.03647
100	0.04137
150	0.04641
200	0.05155
250	0.05676
300	0.06202
350	0.06733
400	0.07266

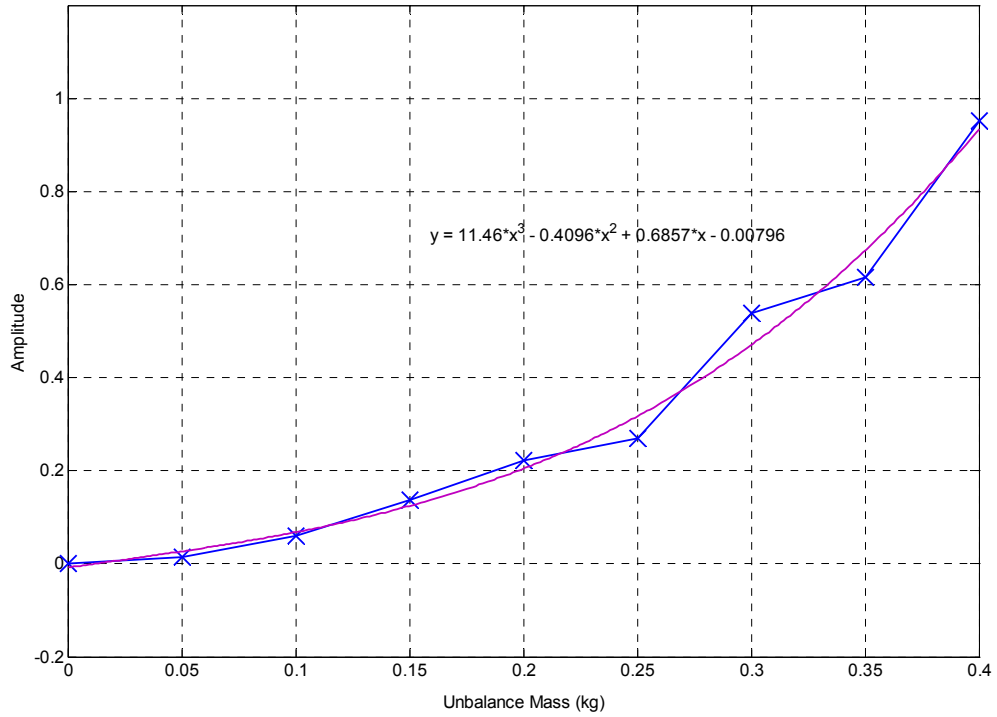


Figure 3.3.1: Motor Current Spectra Value vs. Rotor Unbalance Mass.

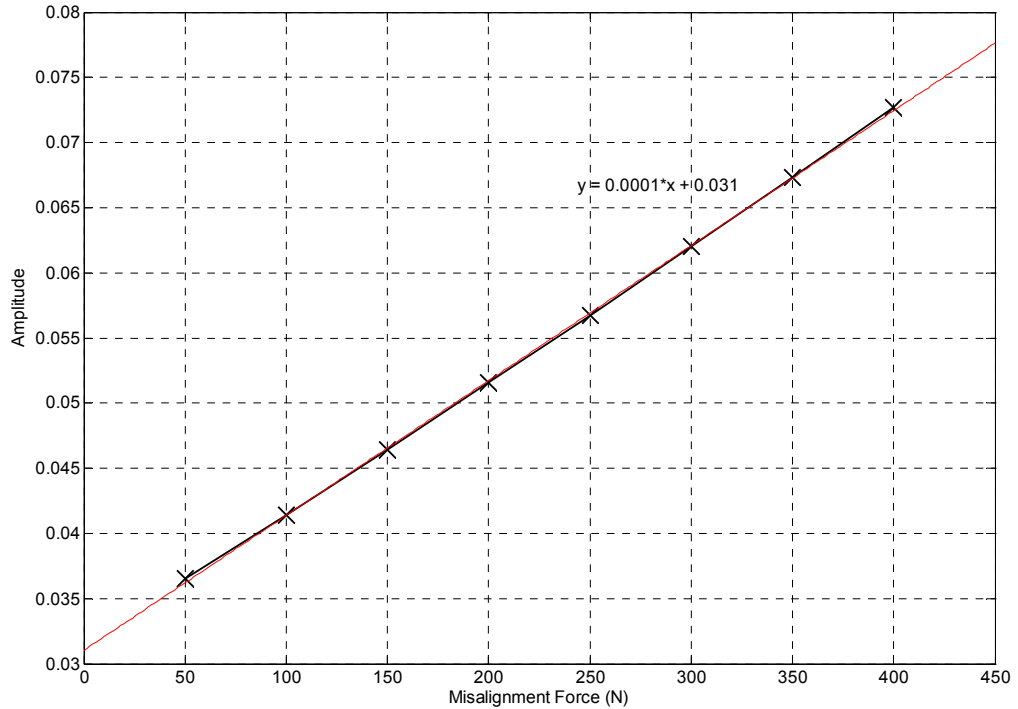


Figure 3.3.2: Motor Current Spectra Value vs. Rotor Misalignment.

CHAPTER FOUR

DISCUSSION OF RESULTS

From the figures presented in chapter 3, the next sections will provide a discussion of the results obtained by running the simulation for the electrical, mechanical and combined system.

4.1 Electrical System Simulation

By referring to figure (3.2.1), the motor speed starts at zero and rises as the voltage is supplied. The speed increases in fractions of a second to oscillate around its steady state value of 1430 rpm, which is achieved after 0.5 seconds.

The next figure (3.2.2) indicates the electromagnetic torque produced by the motor and plotted against time. Unlike the motor speed in the previous figure the torque rises sharply at first and then reverses direction for four cycles and then it continues to fluctuate right until the steady state time value of 0.5 seconds.

Also, figure (3.2.3) indicates the stator current with respect to time. The typical spike of current during startup is quite obvious in the figure as the motor passes the startup phase during the first 0.01 seconds, and then the current heads towards stabilization after 0.2 seconds.

The frequency spectrum of the motor subjected to constant load torque is shown in figure (3.2.4). This figure shows a single frequency spike of 9 Amps at 50 Hz. This frequency is the supply voltage frequency, and this is the only expected value of the current as indicated in figure (3.2.4) at this particular frequency.

At this point it is worth mentioning that the above results are in absolute accordance with the established induction motor behavior.

Figure (3.2.5) is showing the current spectrum of an induction motor subjected to sinusoidal load of amplitude of 25 N.m and frequency of 25 Hz, the spectrum showed two symmetrical side bands *around the current frequency* of 25 Hz which is the load fluctuation frequency, in other words, at the $50 \text{ Hz} \pm 25 \text{ Hz}$ frequencies. This makes logical sense based on energy balance.

Finally, the current spectrum was plotted for an induction motor subjected to sinusoidal load having the same amplitude as the one used in the last two simulation runs shown in the above-mentioned figures, namely 25 N.m, but with at least a twice higher load frequency than the current frequency, let us say 200, 250 and 300 Hz, and the simulation results were plotted in figures (3.2.6a, 3.2.6b and 3.2.6c). The obtained result was a significant addition to this work, as it showed two side bands *around the load torque frequencies*, i.e., 200, 250 and 300 Hz respectively appearing apart from each other by twice the current frequency, 50 Hz. Or in other words, $200 \pm 50 \text{ Hz}$, $250 \pm 50 \text{ Hz}$ and $300 \pm 50 \text{ Hz}$. Similar results are always expected for load torque frequencies higher than twice the current frequency, 50 Hz for the current case.

These results can be explained based on the sum of two trigonometric functions identity as:

$$\sin \alpha + \sin \beta = 2 \sin\left(\frac{\alpha + \beta}{2}\right) \cos\left(\frac{\alpha - \beta}{2}\right)$$

knowing that $\cos(-\alpha) = \cos(\alpha)$

4.2 Mechanical System Simulation

By referring to figure (3.2.5), the input torque is plotted against time. It can be clearly seen that the torque assumes the shape of a ramp wave starting from zero N.m at zero seconds and peaks at 80 N.m at 5 seconds. The torque remains zero up to 25 seconds corresponding to the simulation time interval. This is the torque required for the system to achieve a rotational speed of 3500 rpm.

By integrating the previous ramp function, we obtain figure (3.2.6) which plots as a parabolic function starting from zero rpm (the initial condition) and ends at 3500 rpm according to the theoretical formulation introduced in chapter 2. The end condition of 3500 rpm is maintained as of 5 seconds and holding till the end of the simulation time.

The torsional deflection indicated in figure (3.2.7) is zero at the start of the torque supply at zero seconds, and it sharply dips to -1.1 rads linearly because of the initial torsional inertia. The torsional deflection is then observed to oscillate about the zero mark, exponentially decreasing in magnitude until it assumes a zero value at steady state within around 1 second.

Also the deflection in the x direction of the centroid of the rotor disc is shown in figure (3.2.8). It should be noted that this figure can also indicate the deflection in the y direction as a result of the symmetric shape of the rotor. This fact can be observed by referring to figure (3.2.9). The deflection starts at zero as the motor starts its motion, and as the rotational speed increases, the magnitude of the deflection increases steadily, reaching a maximum value of amplitude around 1660 rpm, where the resonance frequency is located. The amplitude of the deflection starts to decrease after 4 seconds

until it reaches a steady state oscillation of 9.43×10^{-7} m amplitude right until the end of the 25 seconds of simulation time.

Finally, the frequency spectrum of the x direction oscillation is indicated in figure (3.2.10). The figure clearly shows two frequency spikes, one at 27.73 Hz and amplitude 2.6×10^{-7} m and another at 58.29 Hz and 9.43×10^{-7} m amplitude. The first frequency corresponds to the resonance behavior of the rotor, which was also apparent in figure (3.2.8) where the maxima of the deflection in the x direction, while the second frequency corresponds the steady state frequency of the deflection. As a check that the 3500 rpm, which is the value of the steady state rotational speed, is valid, one can divide it by 60 to convert it into Hertz; a value of 58.3 is obtained which is the same as the frequency at the indicated amplitude.

4.3 Combined System Simulation

As for the combined mechanical and electrical system simulation results, the first run was dedicated to show the behavior of a healthy rotor which will be the benchmark for comparison purposes. This is presented in figure (3.2.11), where there appears a single spike in the spectrum at 50 Hz with *no* sidebands appearing. Again, the location of this spike (at 50 Hz) is due to the motor voltage and current frequency.

As was mentioned in section 3.2.3, the rest of the simulations are grouped into two other categories, one group is for the unbalance, then for both unbalance and misalignment.

4.3.1 Unbalanced Rotor Simulation

The mechanical vibration results are shown in figures (3.2.12) and (3.2.13) for vibration magnitudes against time in the X and Y directions, respectively. The vibration in both cases is observed to have started from zero amplitude and then has risen exponentially to the steady state value of 2.24×10^{-3} m. It is worth mentioning there exists a phase shift of 90° between the X and Y vibration components as a result of them being mutually perpendicular.

To obtain the frequency for the vibration, an FFT code run was executed and figures (3.2.14) and (3.2.15) were obtained for X and Y vibrational directions, respectively. The frequency amplitude reached a value of 23.84 Hz, which corresponds to the shaft rotational speed of 1430 rpm. The plane rotation of the shaft is shown in figure (3.2.16).

The results shown in figure (3.2.17) show the motor-stator current spectrum. . The figure shows the unbalance effects and clearly displays two distinct un-identical sidebands. The distance between those sidebands and the current frequency is twice the rotational frequency of the shaft (2X). In this case where the frequency is 50 Hz, the sidebands are located at 2.327 and 97.66 Hz, respectively. The reason why the spikes are not located at exactly 0 and 100 Hz is that the rotating frequency is actually 23.833 Hz not the exact 25 Hz due to induction motor slip. Figure (3.2.18) plots the same results but with the current being plotted on a logarithmic scale. The reason for this is to scale the figure appropriately to clearly show the sidebands.

Figure (3.2.19) replaces the current as the ordinate with the current gain, taken against the 50 Hz current frequency reference. The sidebands are also there, having amplitudes of -142.7 dB @ 2.327 Hz, and -100.7 dB @ 97.66 Hz.

An attempt to investigate the system behavior at lower rotational speeds than 1500 rpm was simulated to emphasize the existence and location of the sidebands. Considering two other induction motors identical to the previous one used, with a different number of poles (8 poles, and 16 poles) rotating at $\frac{1}{2}$ and $\frac{1}{4}$ the full speed of 1500 rpm, respectively. The stator current spectrums were plotted on logarithmic scale against the frequency in figures (3.2.20) and (3.2.21). This run verified the results achieved in the previous simulation in terms of the existence and location of the sidebands (at 2X of the current frequency).

4.3.2 Misaligned and Unbalanced Rotor Simulation

As with the above sequence, the mechanical vibration results are shown in figures (3.2.22) and (3.2.23) for vibration magnitudes against time in the X and Y directions, respectively. The vibration in both cases is observed to have started from zero amplitude and then has risen exponentially to the steady state value of 2.24×10^{-3} m. spike , It is worth mentioning there exists a phase shift of 90° between the X and Y vibration components as a result of them being mutually perpendicular.

As with the unbalance case, to obtain the frequency for the vibration, an FFT code run was executed and figures (3.2.24) and (3.2.25) were obtained for X and Y vibrational directions, respectively. The frequency amplitude reached a value of 23.84 Hz, which corresponds to the shaft rotational speed of 1430 rpm. In figure (3.2.24) a clear spike in the X-direction is found to exist due to the misalignment of the shaft at a frequency of 47.68 Hz with amplitude of 7.418×10^{-5} m. This is the only difference between this case and the one studied in the previous section. Also, the plane rotation of the shaft is shown in figure (3.2.26). This figure differs from figure (3.2.16) in that it has a clear distortion that can be explained by the existence of the misalignment in the shaft.

The results shown in figure (3.2.27) show the motor-stator current spectrum. The figure shows the both effects of unbalance and misalignment in the form of four sidebands that are not identical. Two of the four sidebands have already appeared during the unbalance trials, with the two newly-introduced ones clearly are because of the misalignment effects. Interestingly enough, those two sidebands have the separation of $(1X)$ around the central current frequency. As for the sidebands from the unbalance, the distance between them and the current frequency is, like before, twice the rotational frequency of the shaft $(2X)$. Figure (3.2.28) plots the same results but with the current being

plotted on a logarithmic scale. The reason for this is to scale the figure appropriately to clearly show the sidebands.

Again, figure (3.2.29) replaces the current as the ordinate with the current gain, taken against the 50 Hz current frequency reference. The four sidebands are also there, having amplitudes of -142.7 dB @ 2.327 Hz, and -100.7 dB @ 97.66 Hz for the unbalance sidebands and also -119.0 dB @ 26.17 Hz, and -122.8 dB @ 73.81 Hz for the misalignment sidebands.

The same attempt to investigate the system behavior at lower rotational speeds than 1500 rpm was simulated again with the same aim as to emphasize the existence and location of the sidebands. This also was done by considering two other induction motors identical to the original one used, but with a different number of poles (8 poles, and 16 poles) rotating at $\frac{1}{2}$ and $\frac{1}{4}$ the full speed of 1500 rpm, respectively. The stator current spectrums were plotted on logarithmic scale against the frequency in figures (3.2.30) and (3.2.31). This particular run has produced very interesting results in terms of spikes and sidebands. The sidebands corresponding to the unbalance have remained the same at the same location of 2X, but two more pairs of sidebands can be clearly observed and it is suggested that they are caused by the introduced misalignment, and with different locations corresponding to different poles and rotational speeds. By consulting figure 3.2.30, it can be clearly seen that in addition to the sidebands from unbalance at 2X, and the expected sidebands at 1X from the misalignment, a new pair of sidebands have appeared at 3X away from the current frequency. The plots in figure (3.2.31) emphasizes this result as another pair of sidebands have showed up alongside the ones previously obtained in figure (3.2.30) at a distance of 5X from the current frequency value. This leads to the conclusion that the sidebands resulting from misalignment are expected to occupy the odd numbered multiples of distance away

from the current frequency value (i.e. 1X, 3X and 5X). This result is expected to be significant with the increase of the number of poles in the motor which corresponds to the appropriate speed decrease.

Although the above results may not have a direct application in industry, it nonetheless can provide useful for modeling and diagnostics purposes.

4.4 Parametric Study of Unbalance Mass and Misalignment Force

Simulation

As shown the figure (3.3.1), the motor current spectra is, non-linearly proportional to the mass unbalance value, where the motor current spectra for misalignment is linearly proportional to the misalignment force as can be seen in figure (3.3.2).

Both relations are expected to have a positive slope, as increasing unbalance mass and misalignment force will increase the energy consumed by the induction motor and in turn the current consumed at that unbalance and misalignment specific frequencies, and vice versa.

CHAPTER FIVE

CONCLUSIONS AND RECOMMENDATIONS

5.1 Conclusions

The conclusions achieved from this research thesis can be summarized in the following points based on the produced results:

1. Unbalance in rotors coupled to three phase induction motors can be detected in motor current spectrum as two side bands around the current frequency apart from it by twice the rotating rotor frequency ($2X$), the right hand side frequency spectra is usually higher than the left hand side frequency spectra.
2. Rotors misalignment for rotors coupled to three phase induction motors can be detected in motor current spectrum as two side bands around the current frequency apart from it by the odd rotating rotor frequency ($1X$, $3X$ and $5X$). This result was obtained by running the simulation for an increased number of poles (and hence decreasing rotational speeds) as the span of the spectrum decreases.
3. The value of the current spectra in unbalance case is proportional to unbalance mass value with a non-linear relationship, whereas the spectrum in misalignment case is linearly increasing with misalignment force.
4. Three phase induction motors subjected to variable loads with frequencies higher than the current frequency will show a different spectrum than those subjected to a variable load with a frequency lower than the current frequency; higher frequency load will show two sidebands around the shaft frequency separated from each other by the value of twice the current frequency value.

Loads with frequencies lower than the current frequency will show two side bands around the current frequency separated from the current frequency by the value of the load frequency.

5.2 Recommendations

Motor current signature analysis can be used with confidence to identify rotor unbalance defects as well as rotor coupling misalignment according to this research results.

5.3 Future Work Recommendations

Similar simulations can be carried out for the case of a rotor with multiple discs to represent, for example, a multi-stage rotating machine.

One more thing to investigate is the possible expansion of the current work to include detecting two phase flow (cavitations) in pumps driven by induction motors through motor current signature.

REFERENCES

- Al-Bedoor, B. (2001), **Modeling the coupled torsional and lateral vibration of unbalanced rotors**, Elsevier Science, Computer methods in applied mechanics and engineering, 190 (2001) 5999-6008.
- Al-Bedoor, B., Duyar, A. and Dundics, M. (2005), **Model based expert system for machinery condition monitoring using electrical parameters**. (albedoor@ju.edu.jo).
- Al-Hussain, K. (2003), **Dynamics stability of two rigid rotors connected by a flexible coupling with angular misalignment**, Science Direct, Journal of Sound and Vibration 266 (2003) 217-234.
- Bellini, A., Filippetti, F., Franceschini, G., Tassoni, C., Passaglia, R., Saottini, M., Tontini, G., Giovannini, M. and Rossi, A. (2002). **On-Field experience with online diagnosis of large induction motors cage failures using MCSA**, IEEE transactions on industry applications, vol. 38, no. 4, July / August (2002).
- Benbouzid, M., Vieira, M. and Theys, C. (1999). **Induction motors faults detection and localization using stator current advanced signal processing techniques**, IEEE transactions on power electronics, vol. 14, no. 1, January (1999).
- Benbouzid, M.H. (2000), **A review of induction motors signature analysis as a medium for fault detection**, IEEE Transactions on industrial electronics, vol. 47, no. 5, October (2000).
- Costa, F.F., Almeida, L.A.L., Naidu, S.R., and Braga-Filho, E.R. (2004), **Improving the signal data acquisition in condition monitoring of electrical machines**, IEEE transactions on instrumentation and measurement, vol. 53, no. 4, August (2004).
- Douglas, H., Pillay, P. and Ziarani A.K. (2004), **A new algorithm for transient motor current signature analysis using wavelets**, IEEE Transactions on industry applications, vol. 40, no. 5, September / October (2004).
- Henao, H., Razik, H. and Capolino G.A. (2005), **Analytical approach of the stator current frequency harmonics computation for detection of induction machine rotor faults**, IEEE Transactions on industry applications, vol. 41, no. 3, May / June (2005).
- Jung, J.H., Lee, J.J. and Kwon, B.H. (2006). **Online diagnosis of induction motors using MCSA**, IEEE transactions on industrial electronics, vol. 53, no. 6, December (2006).
- Kar, C. and Mohanty, A. (2004). **Monitoring gear vibration through motor current signature analysis and wavelet transform**, Science Direct, mechanical systems and signal processing 20 (2006) 158–187.
- Kurde, A. (2002). **Online condition monitoring of motor using electrical signature analysis**, presented at the "Recent Advances in Condition-Based Plant Maintenance" seminar organized by Indian Institute of plant Engineers, NITIE, Mumbai, India 17-18 May (2002).

Lees, A. (2007). **Misalignment in rigidly coupled rotors**, Science Direct, Journal of Sound and Vibration 305 (2007) 261-271, May 2007.

Liang, B., Payne, B., Ball, A. and Iwnicki S. (2002), **Simulation and fault detection of three-phase induction motors**, Elsevier Science, Mathematics and computer in simulation 61 (2002) 1-15.

Nandi, S. (2004), **A detailed model of induction machines with saturation extendable for fault analysis**, IEEE transactions on industry applications, vol. 40, no. 5, September / October (2004).

Nandi, S., Toliyat, H.A. and Li, X (2005), **Condition monitoring and fault diagnosis of electrical motors – A review**, IEEE Transactions on energy conversion, vol. 20, no. 4, December (2005).

Okoro, O. (2003), **MATLAB Simulation of induction machine with saturable leaking and magnetizing inductances**, The Pacific Journal of Science and Technology, vol. 5, April 2003.

Penrose, H.W. (2004), **Applications for motor current signature analysis**, All-Test Pro (2004).

Penrose, H.W. (2008), **Electrical Motor Diagnostics**, Success by Design Publishing, second edition, ISBN: 0-9712450-7-X.

Rao, S.S. (1995), **Mechanical Vibrations, Third Edition**, Addison – Wesley Publishing Company, ISBN 0-201-59289-4.

Riley, C.M., Lin, B.K., Habetler, T.G. and Kliman, G.B. (1999). **Stator current harmonics and their causal vibrations: A preliminary investigation of sensorless vibration monitoring applications**, IEEE transactions on industry applications, vol. 35, no. 1, January / February (1999).

Stack, J.R., Habetler T.G. and Harley, R.G. (2004), **Bearing fault detection via autoregressive stator current modeling**, IEEE Transactions on industry applications, vol. 40, no. 3, May / June (2004).

Thomas, W.T. and Gilmore, R.J. (2003), **Motor current signature analysis to detect fault in induction motor drives fundamentals, data interpretation, and industrial case histories**, Proceedings of the thirty-second turbomachinery symposium (2003).

Ye, Z., Wu, B. and Sadeghian, A. (2003), **Current signature analysis of induction motor mechanical faults by wavelet packet decomposition**, IEEE Transactions on industrial electronics, vol. 50, no. 6, December (2003).

إنشاء نموذج كهروميكانيكي و تحليله اهتزازياً للجزء الدوار من المحرك الكهربائي الغير متزن و متخالف المحور.

إعداد
يوسف عدنان يوسف الصمادي

المشرف
الأستاذ الدكتور باسم البدور

ملخص

يعرض هذا البحث نمذجة محرك كهربائي حثي ثلاثي الأطوار موصول مع محور دوار غير متزن وآخر متخالف المحور، تم ربط النموذجين الكهربائي والميكانيكي لكلا الحالتين. جرى التحليل العددي للنماذج باستخدام برنامج تجاري معروف يسمى (ماتلاب / سميولنك) (MATLAB/Simulink). تمت عمليات التحليل باستخدام طريقة تنبؤية تصحيحية لحلول التكامل تسمى طريقة (رنجا كوتا) (Runga-Kutta). أظهرت النتائج أن المحور غير المتزن يظهر تأثيره على طيف تيار الجزء الثابت من المحرك الكهربائي على شكل زوج من الموجات حول تردد التيار وتبتعد كل منها عنه بمقدار ضعف تردد دوران المحور (2X)، في حين يظهر تخالف المحور على شكل زوج من الموجات حول تردد التيار أيضاً ولكن تبعد عنه بمقدار تردد دوران المحور وثلاث أضعافه و خمس اضعافه (1X, 3X, 5X). قيمة الموجات تتناسب طردياً مع قيمة كتلة عدم الاتزان بشكل غير خطي، أما في حالة تخالف المحور فالتناسب طردي أيضاً و لكن بعلاقة خطيه.